Three-Dimensional Lattice Boltzmann Model for Acoustic Waves Emitted by a Source

Jaouad Benhamou, Salaheddine Channouf, Mohammed Jami, Ahmed Mezrhab, Daniel Henry, Valéry Botton

Three-dimensional lattice Boltzmann model for acoustic waves emitted by a source

Jaouad Benhamou[a*], Salaheddine Channouf[a], Mohammed Jami[a], Ahmed Mezrhab[a], Daniel Henry[b] and Valéry Botton[b]

[a]Laboratoire de Mécanique & Energétique, Département de Physique, Faculté des Sciences, Université Mohammed Premier, 60000 Oujda, Morocco.

[b]Laboratoire de Mécanique des Fluides et d'Acoustique, CNRS/Université de Lyon, Ecole Centrale de Lyon/Université Lyon 1/INSA Lyon, ECL, 36 Avenue Guy de Collongue, 69134 Ecully Cedex, France.

[*]Corresponding author: jaouad1994benhamou@gmail.com

Abstract

The present paper implements the lattice Boltzmann method (LBM) to simulate the emission and propagation of sound waves in three-dimensional (3D) situations, with the point source technique used for wave emission. The 3D numerical model is exercised on a benchmark problem, which is the simulation of the lid-driven cavity flow. Tests are then proposed on acoustic situations. The numerical results are first confronted with analytical solutions in the case of spherical waves emitted by a single point source at the center of a cavity. In view of acoustic streaming applications, we then study the case where the waves are emitted from a circular sound source placed at the center of the left boundary of a three-dimensional cavity filled with water. With the circular source discretized as a set of point sources, we can simulate the wave propagation in 3D and calculate the sound pressure amplitude in the cavity. Tests using different emission conditions and LBM relaxation times finally allow us to get good comparisons with analytical expressions of the pressure amplitude along the source axis, highlighting the performance of the lattice Boltzmann simulations in acoustics.

Keywords: lattice Boltzmann method, acoustic waves, point source method, sound pressure, 3D simulation.

1. Introduction

To numerically validate experimental results, the numerical simulation of physical problems in 3D becomes a necessity to visualize the physical phenomena much better than in 2D. The three-dimensional lattice Boltzmann method is chosen in this work to study an interesting problem in engineering: sound wave propagation. This kind of study, especially in the case of ultrasound waves, has been the subject of a large number of theoretical, numerical, and experimental works. Its importance resides in its involvement in many natural, industrial, and medical phenomena, such as interference, reflection, and diffraction processes [1–3], noise [4–6], acoustic separation of fluid particles in a mixture [7,8], photovoltaic silicon purification [9,10], cancer treatment [11–13].

The lattice Boltzmann method is an open-source alternative numerical method for simulating different types of fluid flows. Contrary to the usual approach based on Navier-Stokes equations, the LBM aims

at discretizing the Boltzmann equation, corresponding to statistical modeling of the dynamics of the particles forming the fluid. The origin of LBM generally derives from cellular automata and lattice-gas automata [14–16], and its theory is inspired by statistical physics and the kinetic theory of gases [17–19].

Lattice Boltzmann method is easy to implement and has the advantage of simplicity compared to traditional methods, especially when dealing with complex simulation domains. For this reason, it is used to study the propagation of different types of waves in two and three dimensions. In two dimensions, these studies have been known for a long time in the published literature. For example, different scientific researchers have used the LBM approach to simulate shock waves [20,21] or sound waves [22–24]. In three dimensions, the theory for the study of acoustic propagation by the lattice Boltzmann method has already been stated in previous works [25], but in general, the LBM simulations are not too common for studying the 3D propagation of sound waves in fluids. In contrast, this technique has been widely used for over twenty years to simulate various other physical phenomena, particularly the fluid flows in different geometries [26–28]. Recently, the three-dimensional lattice Boltzmann method has evolved in a very significant way to simulate important physical problems in engineering such as heat transfer processes [29–33] and multiphase flows [34,35].

The present investigation focuses on the study of sound waves generated by a circular sound source by exploiting the three-dimensional lattice Boltzmann approach. Numerically, the source is discretized into a set of sound sources, each of which is modeled with the acoustic point source technique. This technique has been well-known for a long time in the research community. Its mathematical description is well detailed in the references [23,36,37]. Its principle is to generate waves by vibrating a point sound source around its equilibrium position with a sinusoidal variation. The waveform obtained by the simulation at a given time can be visualized on the density field or the pressure field. The sound pressure amplitude can also be calculated by time-averaging the square of the instantaneous pressure. Finally, tests using different emission conditions and LBM relaxation times allow us to get good comparisons with analytical expressions of the pressure amplitude along the source axis, highlighting the performance of the lattice Boltzmann simulations in acoustics.

This scientific document consists of six different sections. In the first part, a general introduction to the research subject is given. The two- and three-dimensional lattice Boltzmann methods are discussed in the second part, whereas the boundary conditions used at the borders of the studied geometry are described in the third part. The validation of the LBM code used is then carried out by studying a reference physical problem: the lid-driven cavity flow. The results concerning the simulation of the acoustic waves are presented in the fifth section, which is the main section. Finally, general conclusions are given in the last section.

2. Lattice Boltzmann method description

The lattice Boltzmann method can be applied with several types of mesh (or lattice), generally cubic or triangular, with a more or less fine discretization of the propagation directions. A popular representation for classifying the different mesh methods is the $DnQm$ scheme. In this case, n determines the dimension of the simulation domain, and m gives the number of propagation directions of the particles composing the fluid. For example, a D3Q15 scheme is a 3-dimensional lattice with 15 directions of fluid-particle propagation. The most used schemes are the following: D2Q9, D3Q15, D3Q19, and D3Q27. Each direction is associated with a velocity vector c_β. In this work, the D2Q9 (Fig.1) and D3Q19 (Fig. 2) schemes are used in 2D and 3D calculations, respectively.

2.1 Two-dimensional MRT-lattice Boltzmann method

For the simulation of the sound waves, Viggen [37] shows that the multiple relaxation time (MRT) LMB scheme is more stable and accurate than the single relaxation time (SRT) model. Thus, in this work, the MRT-LBM technique is chosen to perform the 2D and 3D simulations. For MRT-LBM calculations, the computational fluid evolution is described by the following discretized Boltzmann equation [17,18,38,39]:

$$f_\beta(x_\beta + c_\beta \Delta t, t + \Delta t) = f_\beta(x_\beta, t) + \Omega_\beta \tag{1}$$

where f_β, Δt, c_β and Ω_β represent the distribution functions, the time step, the lattice velocities, and the collision operator, respectively.

The nine LBM velocities c_β of the D2Q9 scheme are

$$c_\beta = \begin{cases} (0,0) & \beta = 0 \\ (1,0)c, (0,1)c, (-1,0)c, (0,-1)c & \beta = 1,\dots,4 \\ (1,1)c, (-1,1)c, (-1,-1)c, (1,-1)c & \beta = 5,\dots,8 \end{cases} \tag{2}$$

where c is the LBM speed between two successive nodes of the lattice.

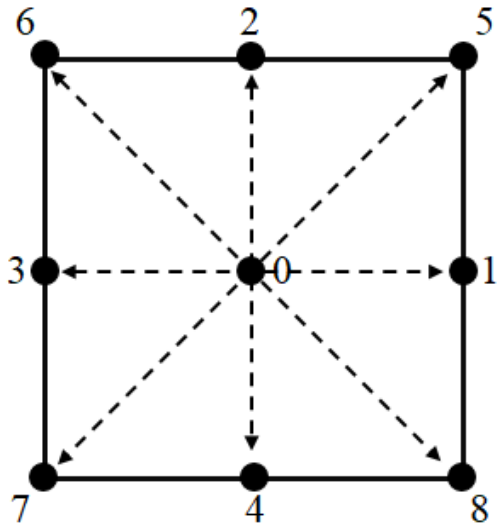

Fig. 1. D2Q9 LBM lattice.

According to the MRT-LBM model, the operator Ω_β is a function of the moments m_β and m_β^{eq}, the inverse matrix M^{-1}, and the collision matrix S:

$$\Omega_\beta = -M^{-1} S [m_\beta - m_\beta^{eq}]. \tag{3}$$

For the D2Q9 model, the matrix S is defined by fixed values of the relaxation times of the computed macroscopic quantities and by the kinematic viscosity (ν). Here, the relaxation times employed are the same as those given in the references [17,24]:

$$S = \mathrm{diag}(1,1.4,1.4,1,1.2,1,1.2,1/(3\nu + 0.5),1/(3\nu + 0.5)) \tag{4}$$

The matrix M and its inverse M^{-1} are described as:

$$m = Mf \text{ and } f = M^{-1}m \tag{5}$$

The matrix M is given as:

$$M = \begin{pmatrix} 1 & 1 & 1 & 1 & 1 & 1 & 1 & 1 & 1 \\ -4 & -1 & -1 & -1 & -1 & 2 & 2 & 2 & 2 \\ 4 & -2 & -2 & -2 & -2 & 1 & 1 & 1 & 1 \\ 0 & 1 & 0 & -1 & 0 & 1 & -1 & -1 & 1 \\ 0 & -2 & 0 & 2 & 0 & 1 & -1 & -1 & 1 \\ 0 & 0 & 1 & 0 & -1 & 1 & 1 & -1 & -1 \\ 0 & 0 & -2 & 0 & 2 & 1 & 1 & -1 & -1 \\ 0 & 1 & -1 & 1 & -1 & 0 & 0 & 0 & 0 \\ 0 & 0 & 0 & 0 & 0 & 1 & -1 & 1 & -1 \end{pmatrix} \tag{6}$$

The vector of moments m_β of the D2Q9 model can be expressed as a function of the fluid density, momentum, energy flux, kinetic energy, and macroscopic components of the stress tensor [24,39].

The vector m_β^{eq} represents the equilibrium moments corresponding to m_β. The mathematical expression of each moment m_β^{eq} is:

$$\begin{aligned} m_0^{eq} &= \rho \\ m_1^{eq} &= -2\rho + 3\rho^2(u^2 + v^2) \\ m_2^{eq} &= \rho - 3\rho^2(u^2 + v^2) \\ m_3^{eq} &= \rho u \\ m_4^{eq} &= -\rho u \\ m_5^{eq} &= \rho v \\ m_6^{eq} &= -\rho v \\ m_7^{eq} &= \rho^2(u^2 - v^2) \\ m_8^{eq} &= \rho^2 uv \end{aligned} \tag{7}$$

where ρ is the density of the simulated fluid, u and v are the macroscopic velocities following the x and y axes, respectively.

2.2 Three-dimensional MRT-lattice Boltzmann method

The Boltzmann equation described above for the 2D simulations (Eq. (1)) is also used in the 3D simulation case. As previously mentioned, the D3Q19 scheme is selected to simulate the propagation of sound waves in three-dimensional geometry. The nineteen lattice velocities $c_\beta = (c_{x,\beta}, c_{y,\beta}, c_{z,\beta})$ of this scheme are:

$$c_\beta = c\begin{pmatrix} 0 & 1 & -1 & 0 & 0 & 0 & 0 & 1 & -1 & 1 & -1 & 1 & -1 & 1 & -1 & 0 & 0 & 0 & 0 \\ 0 & 0 & 0 & 1 & -1 & 0 & 0 & 1 & 1 & -1 & -1 & 0 & 0 & 0 & 0 & 1 & -1 & 1 & -1 \\ 0 & 0 & 0 & 0 & 0 & 1 & -1 & 0 & 0 & 0 & 0 & 1 & 1 & -1 & -1 & 1 & 1 & -1 & -1 \end{pmatrix} \tag{8}$$

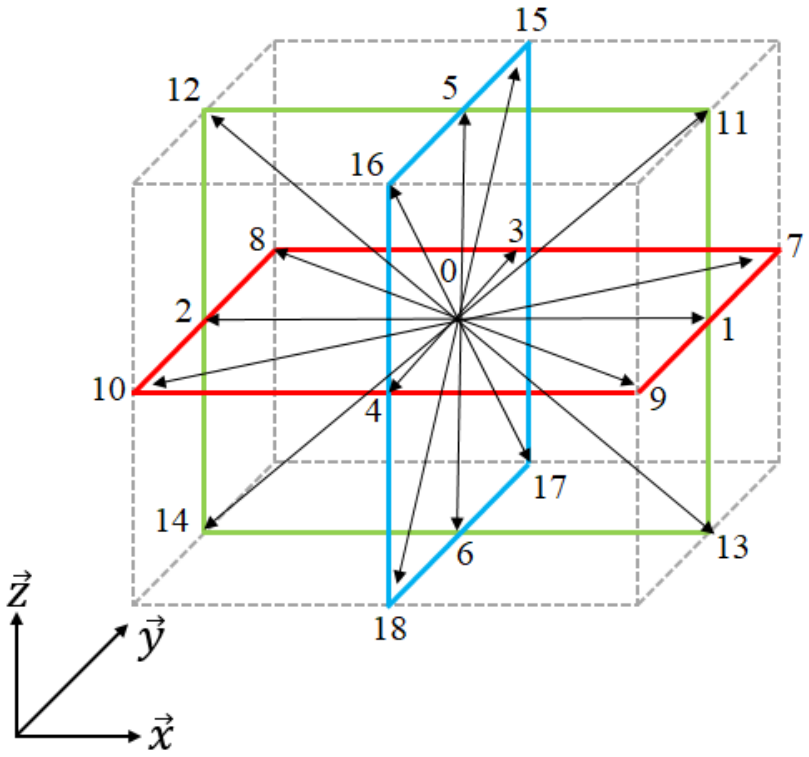

Fig. 2. D3Q19 LBM lattice.

For the D3Q19 scheme, the transformation matrix M is chosen as in the reference [31]. It is given by:

$$M = \begin{pmatrix} 1 & 1 & 1 & 1 & 1 & 1 & 1 & 1 & 1 & 1 & 1 & 1 & 1 & 1 & 1 & 1 & 1 & 1 & 1 \\ -30 & -11 & -11 & -11 & -11 & -11 & -11 & 8 & 8 & 8 & 8 & 8 & 8 & 8 & 8 & 8 & 8 & 8 & 8 \\ 12 & -4 & -4 & -4 & -4 & -4 & -4 & 1 & 1 & 1 & 1 & 1 & 1 & 1 & 1 & 1 & 1 & 1 & 1 \\ 0 & 1 & -1 & 0 & 0 & 0 & 0 & 1 & -1 & 1 & -1 & 1 & -1 & 1 & -1 & 0 & 0 & 0 & 0 \\ 0 & -4 & 4 & 0 & 0 & 0 & 0 & 1 & -1 & 1 & -1 & 1 & -1 & 1 & -1 & 0 & 0 & 0 & 0 \\ 0 & 0 & 0 & 1 & -1 & 0 & 0 & 1 & 1 & -1 & -1 & 0 & 0 & 0 & 0 & 1 & -1 & 1 & -1 \\ 0 & 0 & 0 & -4 & 4 & 0 & 0 & 1 & 1 & -1 & -1 & 0 & 0 & 0 & 0 & 1 & -1 & 1 & -1 \\ 0 & 0 & 0 & 0 & 0 & 1 & -1 & 0 & 0 & 0 & 0 & 1 & 1 & -1 & -1 & 1 & 1 & -1 & -1 \\ 0 & 0 & 0 & 0 & 0 & -4 & 4 & 0 & 0 & 0 & 0 & 1 & 1 & -1 & -1 & 1 & 1 & -1 & -1 \\ 0 & 2 & 2 & -1 & -1 & -1 & -1 & 1 & 1 & 1 & 1 & 1 & 1 & 1 & 1 & -2 & -2 & -2 & -2 \\ 0 & -4 & -4 & 2 & 2 & 2 & 2 & 1 & 1 & 1 & 1 & 1 & 1 & 1 & 1 & -2 & -2 & -2 & -2 \\ 0 & 0 & 0 & 1 & 1 & -1 & -1 & 1 & 1 & 1 & 1 & -1 & -1 & -1 & -1 & 0 & 0 & 0 & 0 \\ 0 & 0 & 0 & -2 & -2 & 2 & 2 & 1 & 1 & 1 & 1 & -1 & -1 & -1 & -1 & 0 & 0 & 0 & 0 \\ 0 & 0 & 0 & 0 & 0 & 0 & 0 & 1 & -1 & -1 & 1 & 0 & 0 & 0 & 0 & 0 & 0 & 0 & 0 \\ 0 & 0 & 0 & 0 & 0 & 0 & 0 & 0 & 0 & 0 & 0 & 0 & 0 & 0 & 0 & 1 & -1 & -1 & 1 \\ 0 & 0 & 0 & 0 & 0 & 0 & 0 & 0 & 0 & 0 & 0 & 1 & -1 & -1 & 1 & 0 & 0 & 0 & 0 \\ 0 & 0 & 0 & 0 & 0 & 0 & 0 & 1 & -1 & 1 & -1 & -1 & 1 & -1 & 1 & 0 & 0 & 0 & 0 \\ 0 & 0 & 0 & 0 & 0 & 0 & 0 & -1 & -1 & 1 & 1 & 0 & 0 & 0 & 0 & 1 & -1 & 1 & -1 \\ 0 & 0 & 0 & 0 & 0 & 0 & 0 & 0 & 0 & 0 & 0 & 1 & 1 & -1 & -1 & -1 & -1 & 1 & 1 \end{pmatrix} \tag{9}$$

The vector m_β can be written as a function of the density (ρ), the kinetic energy (e) and its square (e^2), the momentum ($j = (j_x, j_y, j_z)$), and the three elements of the energy flux (q_x, q_y, q_z). The remaining quantities are p_{xx}, p_{xy}, p_{yz}, and p_{zx}, which are the constituents of the symmetrical traceless viscous

stress tensor, and π_{xx} and π_{ww}, which have the same symmetry as the diagonal part of the traceless viscous tensor p_{ij}. The other two normal components of the viscous stress tensor p_{yy} and p_{zz} can be used to construct $p_{ww} = p_{yy} - p_{zz}$. There are three missing quantities m_x, m_y, and m_z which are parts of a third rank tensor [28,40]:

$$m = \left(\rho, e, e^2, j_x, q_x, j_y, q_y, j_z, q_z, 3p_{xx}, 3\pi_{xx}, p_{ww}, \pi_{ww}, p_{xy}, p_{yz}, p_{zx}, m_x, m_y, m_z\right)^T \quad (10)$$

The nineteen equilibrium moments m_β^{eq} can be expressed as a function of the fluid density and the impulsions j_x, j_y, j_z [29]. The calculation of the vector m^{eq} can be directly given by:

$$m^{eq} = Mf^{eq} \quad (11)$$

where f^{eq} is the equilibrium function. f^{eq} is expressed as a function of density, speed of sound (c_s), macroscopic velocity vector $\vec{V} = (u, v, w)$, velocities of the D3Q19 lattice (c_β) and discretization weights (W_β):

$$f_\beta^{eq} = W_\beta \rho\left[1 + \frac{1}{c_s^2}\,\vec{c}_\beta.\vec{V} + \frac{1}{2c_s^4}\left(\vec{c}_\beta.\vec{V}\right)^2 - \frac{1}{2c_s^2}\left|\vec{V}\right|^2\right], \text{ with } \beta = 0, \dots, 18 \quad (12)$$

The nineteen factors W_β are:

$$W_\beta = \begin{cases} \frac{1}{3} & \beta = 0 \\ \frac{1}{18} & \beta = 1, \dots, 6 \\ \frac{1}{36} & \beta = 7, \dots, 18 \end{cases} \quad (13)$$

The relaxation matrix S can be written as:

$$\mathrm{S} = \mathrm{diag}(s_0, s_1, s_2, s_3, s_4, s_5, s_6, s_7, s_8, s_9, s_{10}, s_{11}, s_{12}, s_{13}, s_{14}, s_{15}, s_{16}, s_{17}, s_{18}) \quad (14)$$

s_0, s_3, s_5, and s_7 are the relaxation parameters corresponding to the macroscopic quantities ρ, j_x, j_y, and j_z, respectively. They often take the values 0 or 1. In this work, they are fixed to the value of unity. The parameters s_9, s_{11}, s_{13}, s_{14} and s_{15} are linked to the LBM kinematic viscosity ν as $s_9 = s_{11} = s_{13} = s_{14} = s_{15} = 1/(3\nu + 0.5)$. For the relaxation time s_1, it is advised to fix it at 1.19 [29]. Otherwise indicated, it is the value we have chosen. The remaining parameters (s_2, s_4, s_6, s_{10}, s_{12}, s_{16}, s_{17} and s_{18}) are the free parameters [40].

3. Boundary conditions

The boundary conditions adopted in this paper are bounce-back (BBC) and non-reflecting (NRBC) conditions. The BBC conditions are generally used to compute the unknown distribution functions at the solid boundary (solid node). They are expressed as

$$f_\beta(\vec{x}_{wall}, t) = f_{\bar{\beta}}(\vec{x}_{wall}, t), \quad (15)$$

where $f_\beta(\vec{x}_{wall}, t)$ is an unknown distribution function at the wall node ($\vec{x}_{wall}$) and $f_{\bar{\beta}}(\vec{x}_{wall}, t)$ is the known function at the opposite direction ($\bar{\beta} = -\beta$).

For the NRBC conditions, there are different techniques to absorb waves at boundaries, such as characteristic boundary conditions or the use of an absorbing layer [18,41]. In the present work, a simple boundary condition, which is a modified bounce-back boundary condition [42], is used to attenuate the waves:

$$f_{\bar{\beta}} = f_{\beta} - 3\,\rho_a\,W_{\beta}\,c_{\beta}\,sin(\omega t - kx)\,e^{-\alpha\,x}, \tag{16}$$

where the parameters ρ_a, W_{β}, ω, t, x, α and k are the amplitude of the sound source, the discretization weights, the angular frequency, the time, the distance between the source and the absorbing boundary, the spatial attenuation coefficient, and the wavenumber, respectively. The mathematical expression of α is given in section 5.

After determining the collision and the streaming processes and implementing the boundary conditions, the physical quantities ρ and j can be calculated as:

$$\rho = \sum_{\beta=0}^{q} f_{\beta},\ j(x,y,z) = \sum_{\beta=0}^{q} f_{\beta}\,c_{\beta}, \tag{17}$$

where q is the number of discretized LBM velocities ($q = 8$ in the 2D case or $q = 18$ in the 3D case).

4. D3Q19-LBM model validation

In general, fluid dynamics in closed cavities is technically and scientifically a fundamental problem in the fluid mechanics discipline. Moreover, it has received significant attention for many years, not only for the convenience of using simple geometries, but also for its practical importance to investigate many different physical phenomena such as vortex dynamics, hydrodynamic stability, and flow bifurcation. For all these reasons, the lid-driven cavity problem has been widely used for testing or validating new codes or new numerical simulation methods. The validation in our study will be done by comparing our results on this problem with those given in the references [43–45]. This work focuses on a closed cubic cavity that is filled with an incompressible viscous fluid (a good approximation for water). The upper wall is moved with a uniform translation velocity ($u_0 = 0.1$), while the other walls are fixed and submitted to bounce back (no-slip) boundary conditions (see Fig.3). The Reynolds number is defined by the lid velocity u_0, the cavity length L and the kinematic viscosity ν ($Re = L\,u_0/\nu$), and it varies from 100 to 1000.

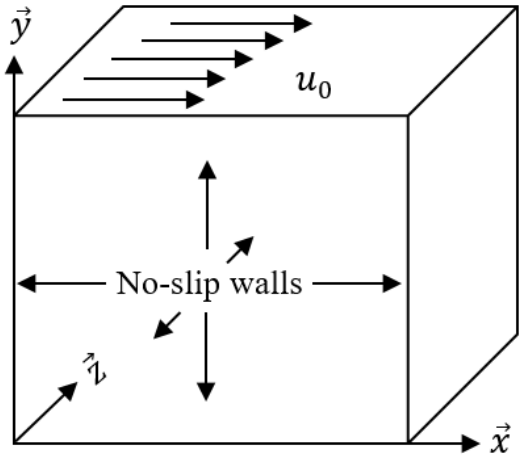

Fig. 3. Sketch of the validation problem.

Numerically, to have a lid-driven cavity flow using the lattice Boltzmann method, the boundary conditions for moving walls proposed by Bouzidi et al. [46] can be used (see also the reference [47]). These conditions consist in modifying the bounce-back boundary conditions by adding the velocity of the moving wall (u_0) in the following way:

$$f_{\bar{\beta}} = f_{\beta} - 2\, W_{\beta}\, c_{\beta}\, \frac{u_0}{c_s^2}. \tag{18}$$

A first validation with the results of Ku et al. [43], Jiang et al. [44], and Ding et al.[45] is shown in Figs. 4-6. These figures depict the dimensionless velocities along the x axis, $U = u/\,u_0$, and along the y axis, $V = v/\,u_0$, by giving profiles along midlines for different Reynolds numbers. It can be noted that the velocity U is equal to zero at the bottom wall and reaches the velocity $U_0 = 1$ imposed at the top wall (moving lid), whereas the velocity V at the bottom and top walls is equal to 0. The flow intensity in the core is found to increase with the increase of the Reynolds number. In any case, a good agreement is found between our current LBM results and the previous benchmark results, even for the larger value of Re ($Re = 1000$, Fig. 6).

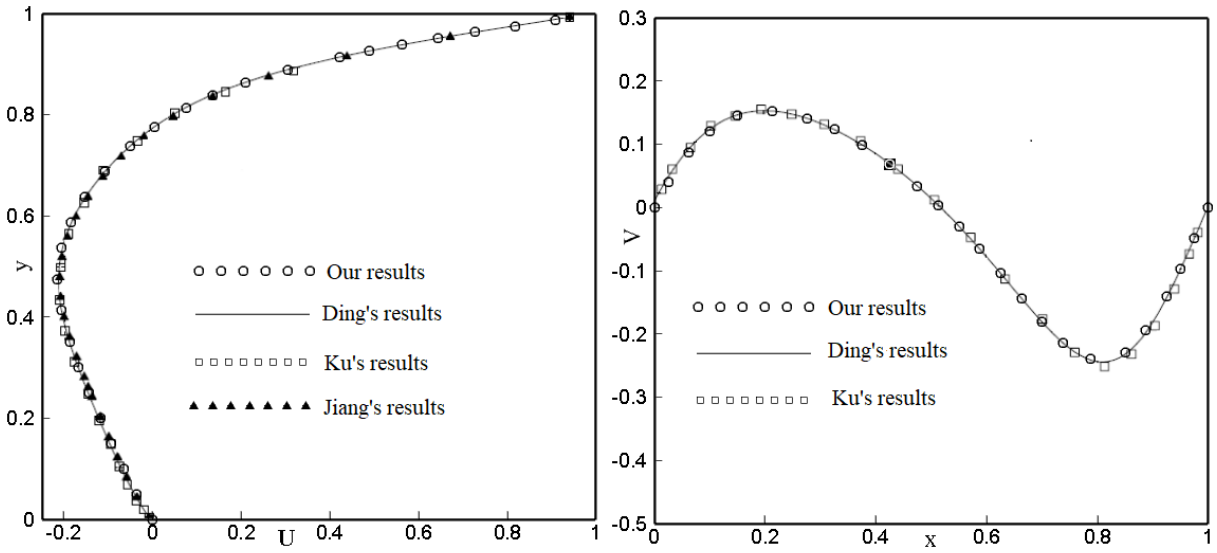

Fig. 4. U and V velocity profiles along the cavity midlines for the lid-driven cavity at $Re = 100$.

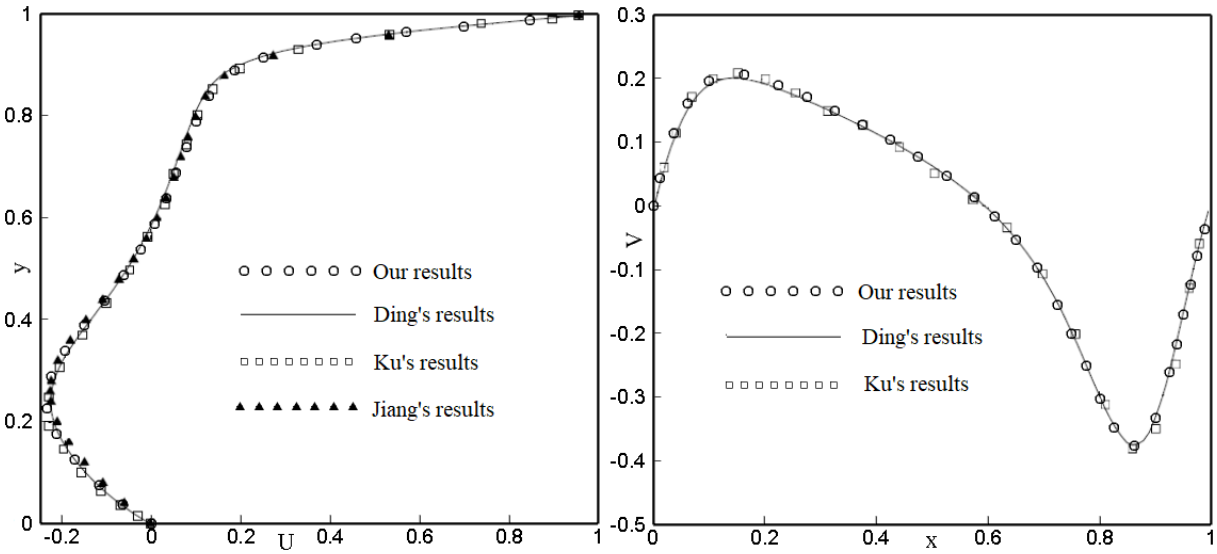

Fig. 5. U and V velocity profiles along the cavity midlines for the lid-driven cavity at $Re = 400$.

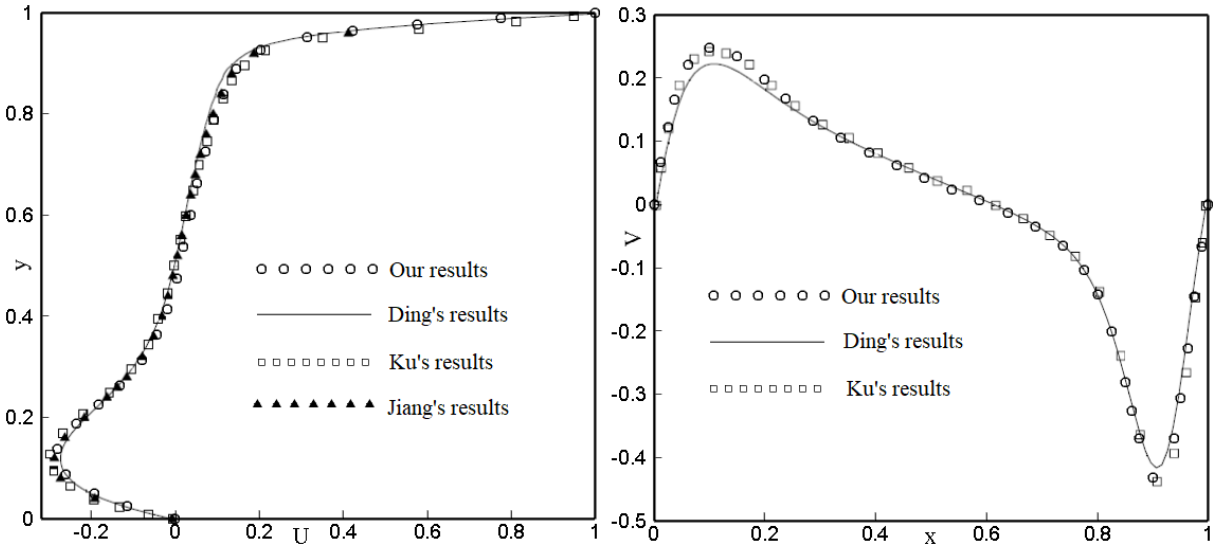

Fig. 6. U and V velocity profiles along the cavity midlines for the lid-driven cavity at $Re = 1000$.

As a complement to this validation, we propose to compare the streamlines found in the lid-driven cavity by our LBM simulation (Fig. 7) with those obtained by Wang et al. [48] (Fig. 8). The Reynolds number for this comparison is fixed at $Re = 400$ and the streamlines are plotted in the main central planes of the three-dimensional cavity. In the longitudinal $z = 0.5$ plane (Fig. 7(a)), we clearly see that the flow follows the moving lid to the right in the upper part, goes down at the right wall, moves to the left in the lower part, and finally goes up to the upper wall along the left wall. The center of the vortex that is thus created is located in the upper right region, but progressively moves towards the center of the cavity as the Reynolds number is increased. Note that counter-rotating vortices appear in both lower corners of the cavity. In the $x = 0.5$ (Fig. 7(b)) and $y = 0.5$ (Fig. 7(c)) planes, streamlines connected with the main vortex and to pressure effects induced by the involved rotation are obtained. In all these planes, we obtain the same hydrodynamic behavior as Wang et al. [48] (Fig. 8), which shows the reliability and accuracy of our numerical model (D3Q19 LBM scheme). In the next section, additional validations will be given in the case of acoustic problems through comparisons with analytical results.

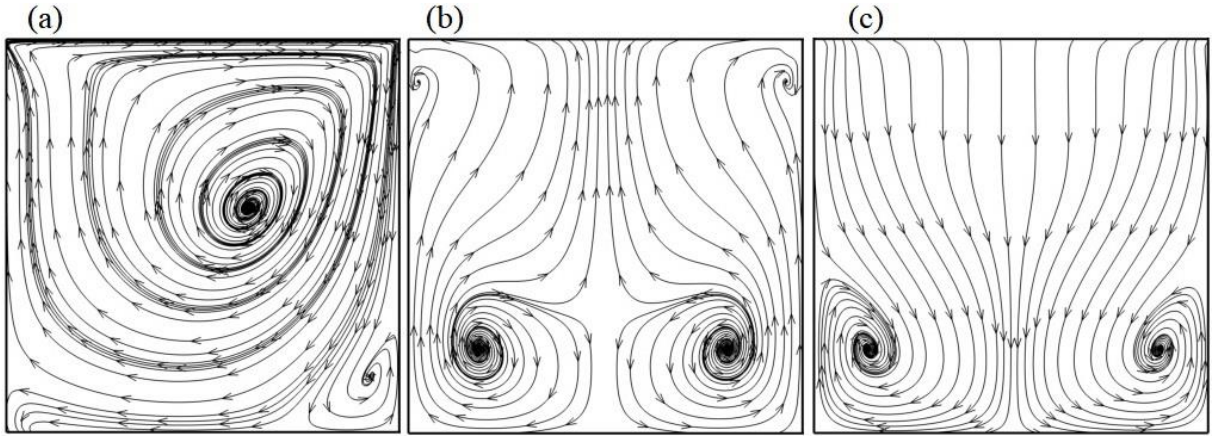

Fig. 7. Streamlines obtained by our LBM simulation for the lid-driven cavity at $Re = 400$; (a): $z = 0.5$, (b): $x = 0.5$, and (c): $y = 0.5$.

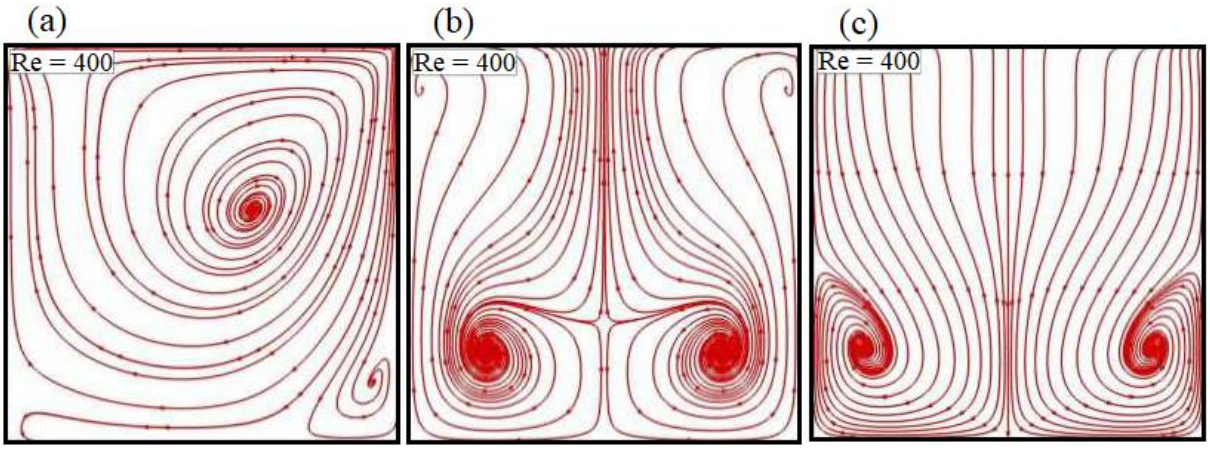

Fig. 8. Streamlines results of reference [48] for the lid-driven cavity at $Re = 400$; (a): $z = 0.5$, (b): $x = 0.5$, and (c): $y = 0.5$.

5. Results and discussion

Three-dimensional (3D) numerical studies of the waves propagation in water are performed using the lattice Boltzmann method (LBM) associated with the multiple relaxation time (MRT) model and the results are presented in this section. The waves are emitted from a circular sound source placed at the center of the left boundary of a 3D cavity using the acoustic point source (APS) technique. In 2D, this technique has been widely addressed by many researchers [23,37,49] using the single relaxation time model. However, according to [37], the investigation of the wave behavior with the MRT model is more stable and accurate than with the SRT model. In the present work, the powerful 2D MRT-LBM model, developed for wave simulation and used in our previous two-dimensional works [24,50], is adapted to take into account more realistic 3D configurations.

5.1 Physical problem description and mathematical formulation

The physical problem studied in this work is the propagation of acoustic waves in a simple parallelepipedic cavity with rigid plane walls and filled with water. The waves are emitted by a circular vibrating sound source located at the center of the left vertical wall (at $x = 0$). This source vibrates at a frequency of 200 kHz. The spatial dimensions of the cavity are the length, the width, and the height, which are denoted as L, W, and H, respectively, with $W = H$ (see Fig.9). The wall opposite to the sound source (at $x = L$) is an absorbing wall. The non-reflecting boundary conditions described in section 3 are applied to this wall. In contrast, the bounce back-boundary conditions are applied at the other walls, which are sound-reflecting.

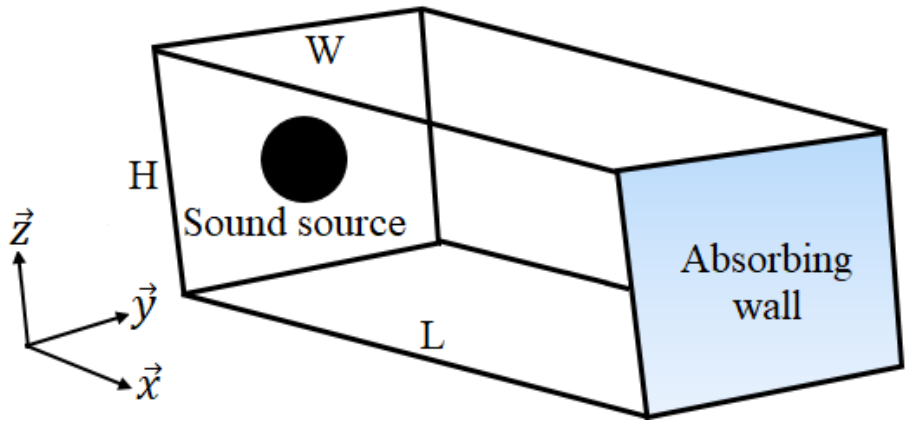

Fig. 9. The physical problem studied.

The waves propagate in water, which is considered as homogeneous throughout the confined cavity, with constant thermophysical properties. Physically, the travel of an acoustic wave through a fluid (water) creates small perturbations in pressure, density, and velocity. These perturbations [36] are expressed by:

$$p(r,t) = p_0 + p'(r,t), \tag{19}$$

$$\rho(r,t) = \rho_0 + \rho'(r,t), \tag{20}$$

$$u(r,t) = u_0 + u'(r,t), \tag{21}$$

where the quantities p', ρ', and u' are small fluctuations, and the parameters p_0, ρ_0, and u_0 ($u_0 = 0$) are the pressure, density, and velocity of the undisturbed fluid (fluid at rest). In these expressions, r and t refer to the dependence on space and time.

The points of the cavity discretization belonging to the circular source are considered as point sources, according to the acoustic point source method [23,24,37]. This method can be highlighted by considering fluctuations of the density (Eq. (20)). In this case, we generate the waves by vibrating the fluid density at the position of each point source, and the quantity ρ' can then be expressed by the following sine function:

$$\rho' = \rho_a \sin(\omega t), \tag{22}$$

where the parameters ρ_a and ω represent the amplitude and the angular frequency, respectively.

The circular sound source is located at the center of the left wall, i.e. at $x = 0, y = z = H/2$, and it is defined by its radius a. For the APS method in 3D, the waves emitted by each point source propagate as spherical waves. Analytically, these waves can be described by the solution of the linear wave equation. Thus, for spherically symmetric density fields, the analytical solution is

$$\rho'(r,t) = \frac{A}{r} e^{j(\omega t - kr)}, \tag{23}$$

where r is the radial distance from the point source, k is the wavenumber, and A is a constant.

In their work on the investigation of sound waves propagation, Salomons et al. [23] have shown that high values of fluid viscosity can lead to high sound dissipation. For insignificant thermal effects (as is the case in water), the effect of wave dissipation in the fluids can be effectively described by the attenuation coefficient α, which is defined as

$$\alpha = \frac{1}{2}\, \omega^2 \left(\frac{4}{3}\nu + \nu_B\right) c_s^{-3}, \tag{24}$$

where ν_B is the bulk viscosity (for water, $\nu_B = 3\nu$) [9,36].

To consider the effect of dissipation in the analytical solution, it is necessary to introduce a complex wavenumber involving the attenuation coefficient α, as in the references [23,24]:

$$k = \frac{2\pi}{\lambda} - j\alpha. \tag{25}$$

From equations (23) and (25), the real analytical solution is now expressed by:

$$\rho'(r,t) = \frac{A}{r}\cos(\omega t - \frac{2\pi}{\lambda}r)e^{-\alpha r}. \tag{26}$$

This analytical solution for a single point source will be used as the first test of our numerical method. This is discussed in detail in the next sub-section.

It is worth mentioning that the lattice Boltzmann method is a completely non-dimensional technique. However, carrying out physical simulations can impose some constraints on the real units. It is then important to refer to the adequate conversion between LBM and physical units, as it is done in references [37,49]. In LBM units, the dimensions of the cavity and the source diameter ($d = 2a = H/3$) are defined by the numbers of points N of the LBM lattice (points from 0 to N). Physically, the points defining the simulation grid are separated by a specified distance Δx (m), and the particles constituting the fluid require a time Δt (s) to migrate from one node to another. These two quantities Δx and Δt are the references for space and time, respectively, and are generally used to perform the conversion. For example, the LBM wavelength (λ_{lbm}) and period T_{lbm} can be simply calculated as:

$$T_{lbm} = \frac{T_{ph}}{\Delta t} \text{ and } \lambda_{lbm} = \frac{\lambda_{ph}}{\Delta x}, \tag{27}$$

where the indexes lbm and ph are used to refer to LBM and physical quantities, respectively. As mentioned before, the vibration frequency is 200 kHz. For a speed of sound in the water of $c_{ph} = 1480$ m/s, this frequency leads to a wavelength of 0.74 cm and a period of 5 μs. To ensure that the wave propagation through the cavity is accurately simulated, at least 20 Δx should be selected for a single wavelength. This led us to the choice of $\Delta x = 0.032$ cm. The parameter Δt can then be easily determined from the equation mentioned in references [23,37]:

$$\Delta t = \frac{c_{lbm}}{c_{ph}}\Delta x, \tag{28}$$

where c_{lbm} is the speed of sound in LBM units ($c_{lbm} = 1/\sqrt{3}$ for D2Q9 and D3Q19 models). We obtain $\Delta t \approx 0.125$ μs. Note that the LBM time will be denoted as t in the following: as an example, $t = 100$ corresponds to a physical time of 100 Δt.

Using these reference quantities, the values of T_{lbm} and λ_{lbm} are 40.0536 and 23.125, respectively. The LBM angular frequency can also be easily determined from the LBM period ($\omega_{lbm} = 2\pi/T_{lbm}$). The number of points taken to simulate the cavity is $N = 240$ along the z and y axes ($H = W = 240$) and $N = 320$ along the x axis ($L = 320$). Then, the diameter of the circular source corresponds to 81 point sources. Note that the point sources are those of the lattice belonging to the circular source area, so that they are not axisymmetrically disposed.

It is well known that the waves attenuate under the effect of dissipation and geometric spreading. As mentioned before, in water, the effect of dissipation is due to the fluid viscosity. The LBM viscosity ν_{lbm} can be directly determined from the real viscosity ν_{ph} using

$$\nu_{lbm} = \nu_{ph}\,\frac{c_{lbm}}{c_{ph}\,\Delta x}. \tag{29}$$

5.2 Acoustic point source method validation and boundary conditions verification

A first test concerning the propagation of the wave and its interaction with the cavity walls is carried out. Figs. 10-12 represent the numerical results obtained for waves generated by a point acoustic source at the center of a cubic cavity filled with water. These results are taken at two different times. We observe that the waves propagate in the form of spheres, with a radius increasing with the number of iterations (Figs. 10(A), 11(A), and 12(A)). Vertical sections at $y = W/2$ are plotted in Figs. 10(B), 11(B), and 12(B) to illustrate the waveform in two dimensions, which appears as circles. For a small number of iterations ($t = 100$ for example), the waves propagate in the cavity without reaching the boundaries (Fig. 10). When the waves encounter surfaces where the bounce-back conditions (15) are applied (Fig. 11), significant reflections of the waves are noticed: the reflected waves meet the waves emitted by the source, and interferences are then produced. In contrast, when the absorbing boundary conditions (16) are applied on all the walls (Fig.12), the waves appear to be well absorbed by the cavity walls as almost no interference can be noted. These results are a good validation of the BBC and NRBC boundary conditions.

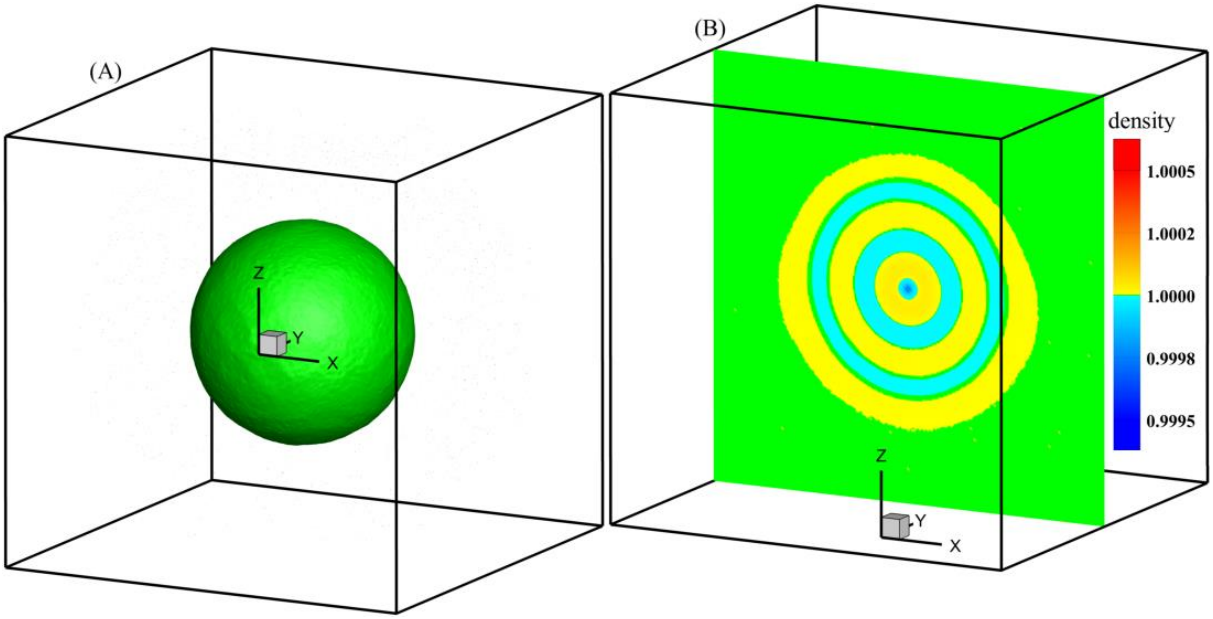

Fig. 10. Propagation of sound waves generated by a single point source: numerical result expressed with the density field at $t = 100$; (A) 3D representation; (B) 2D representation for a vertical section at $y = W/2$.

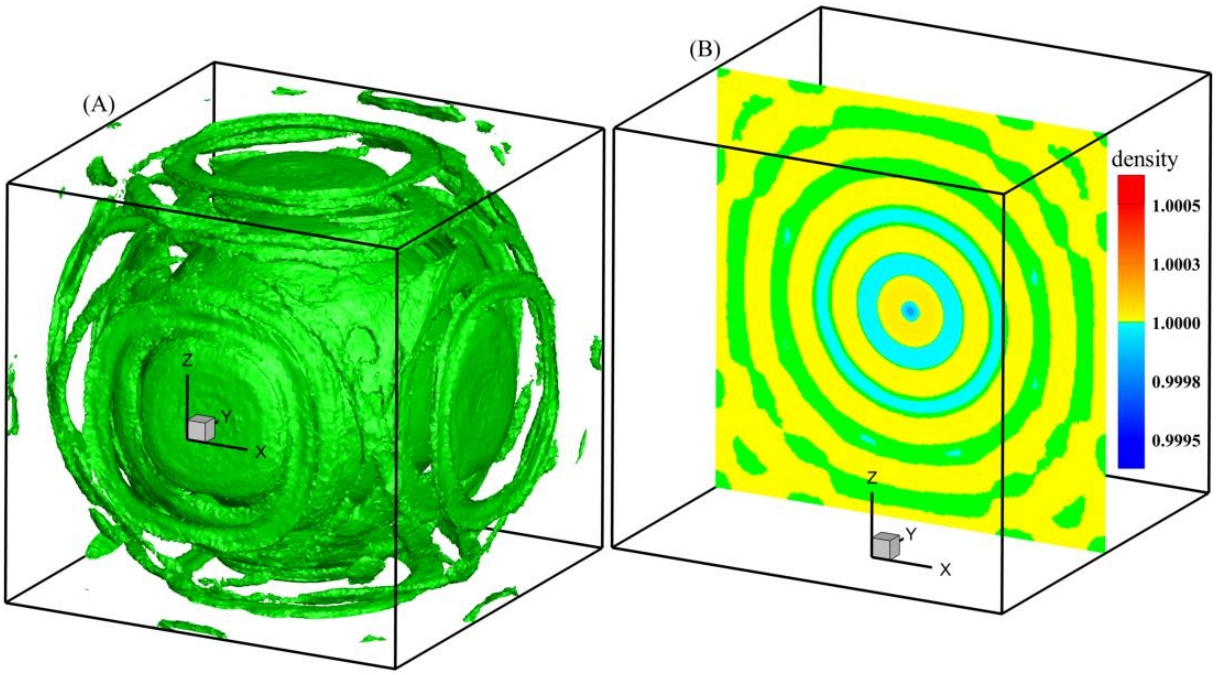

Fig. 11. Propagation of sound waves generated by a single point source: numerical result expressed with the density field at $t = 260$, in the case of BBC boundary conditions; (A) 3D representation; (B) 2D representation for a vertical section at $y = W/2$.

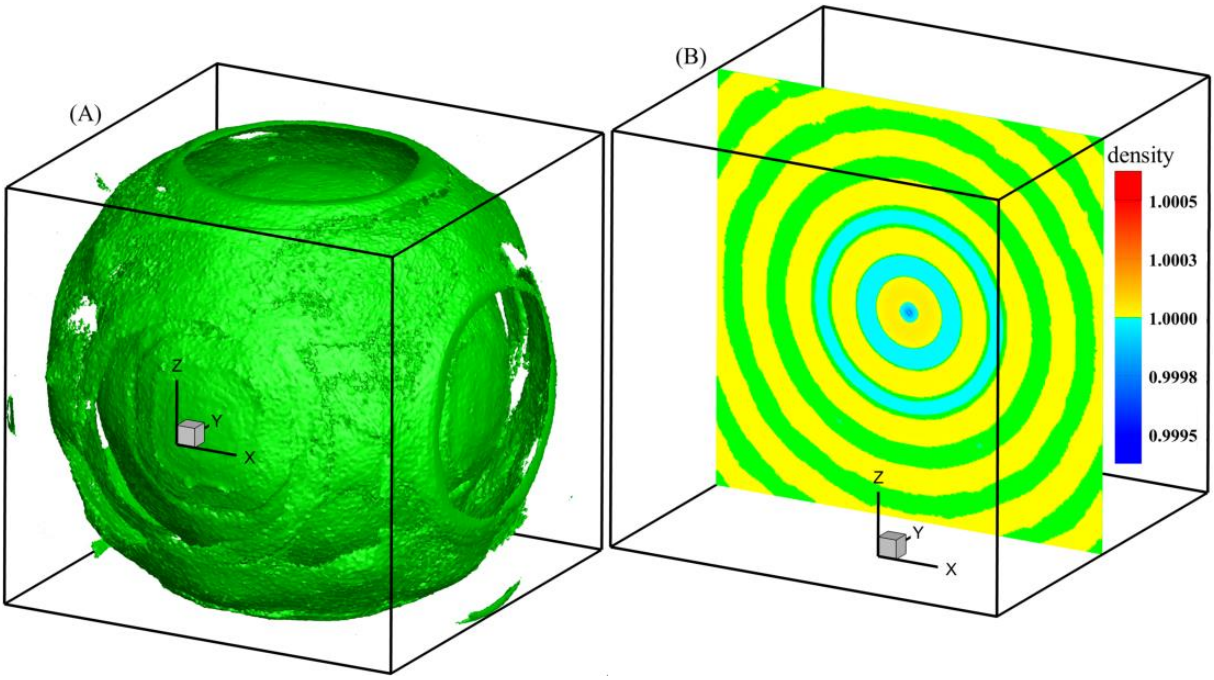

Fig. 12. Propagation of sound waves generated by a single point source: numerical result expressed with the density field at $t = 260$, in the case of NRBC boundary conditions; (A) 3D representation; (B) 2D representation for a vertical section at $y = W/2$.

For comparison, the analytical solution of equation (26) is shown in Fig. 13. This equation being undefined at the center of the cavity ($r = 0$), the analytical density at this point is assumed to be equal to the numerical density. For all types of waves (plane, cylindrical or spherical), a constant factor A appears in the analytical solution of the ideal wave equation [36]. For the case of cylindrical waves, previous 2D studies [23,24,37,50] have shown that a good correspondence with the numerical results

can be obtained when A is a function of the perturbation amplitude ρ_a. Similarly, in the present study, a close correspondence is obtained for $A = 0.04\rho_a$. Fig. 13(A) shows the 3D analytical density field, with a nice spherical shape, in close correspondence with what was obtained numerically in Fig. 12(A). This correspondence is still more clearly noticed from the vertical sections shown in Figs. 12(B) and 13(B). Note that the LBM points used to get the results in Figs. 10-13 are 200 nodes along x, y and z axes ($L = W = H = 200$).

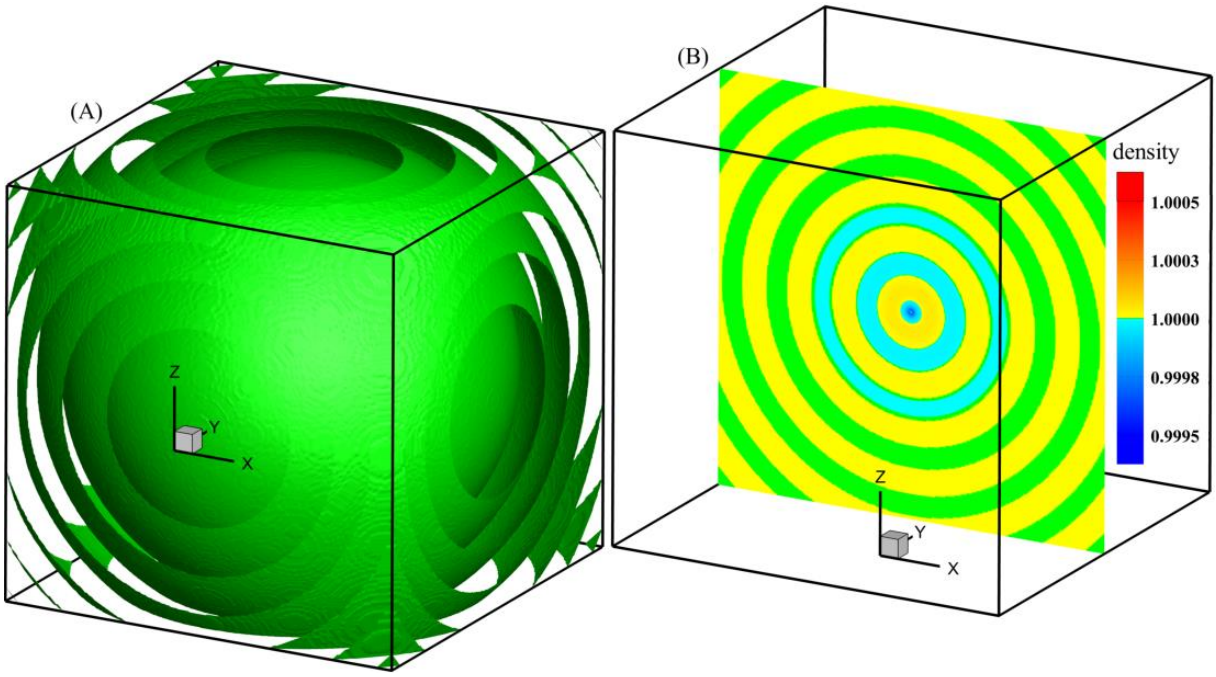

Fig. 13. Propagation of sound waves generated by a single point source: analytical result expressed with the density field at $t = 260$; (A) 3D representation; (B) 2D representation for a vertical section at $y = W/2$.

A good agreement in terms of waveforms was noted between the density shapes obtained analytically and numerically (Figs. 12 and 13). For a more quantitative comparison, the analytical and numerical density profiles are plotted along the central x axis (see Fig. 14(A)). These longitudinal profiles are very similar to each other. The absolute error (Ea) between the two results, shown in Fig. 14(B), appears to vary between 0 and 6.5 10^{-5}, its amplitude decreases with the distance x from the point source. The main error is in fact located on two peaks, in a small area near the center of the cavity, so that the two calculations can be considered as very close. This can be well illustrated by computing the mean error Em of Ea. The value found for Em is relatively low, about 4 10^{-6}. It must be noted, however, that the adjustment of the analytical results with the numerical results has only been done roughly, without real optimization, through the factor of 0.04 ρ_a involving a single figure, and, contrary to previous 2D comparisons [37,50], without introducing a phase shift. As seen in figure 14(A), a slight phase shift and a more precise value of the factor would really improve the comparisons. This was not the main objective of our study. These different tests show that the APS technique and the boundary conditions can be considered as well validated and the LBM code is now ready for the simulation of the problem shown in Fig. 9.

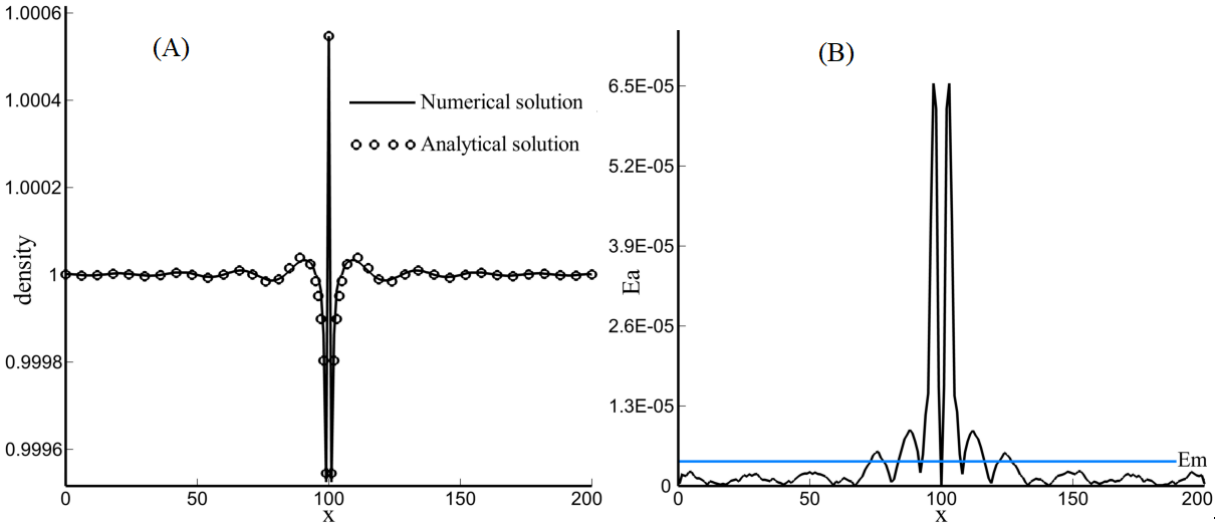

Fig. 14. Longitudinal profiles of the analytical and numerical densities along the central x axis at $t = 260$ in the case of sound waves generated by a single point source (A) and the variation of the absolute error between them (B).

5.3 Acoustic field emitted by a circular acoustic source

We now consider the problem of sound waves generated by a circular acoustic source, the problem described in section 5.1 and sketched in Fig. 9. We first consider the case where the sound waves are due to density fluctuations applied at the source. For this case, the LBM simulations are performed with a LBM kinetic viscosity of 0.01 and $s_1 = 1.19$. These choices are discussed later. In a second step, we will propose to consider velocity fluctuations at the source.

5.3.1 Density fluctuations applied at the source

Fig. 15 illustrates the sound waves generated by density fluctuations applied at the circular acoustic source (Fig. 9) through the plot of the density field after 1100 iterations. The interference between the spherical waves emitted by each point source creates an acoustic beam in the cavity. This beam is well directed towards the absorbing endwall. As can be seen in Fig. 15(A), the density field is not perfectly axisymmetric around the central x axis (the symmetry axis of the source), as it ought to be with a circular acoustic source. It can be explained by the fact that the discretization of the source by point sources is not axisymmetric. On the vertical section of the density field shown in Fig. 15(B), we can see that the resulting waves have not a spherical shape near the source, but rather a flat central front and curved sides. The maximum wave amplitudes are found in this near field zone, on the central x axis or on both sides of it, a characteristic of the complex near field zone. As expected, the spherical shape of the waves can only be observed in the far-field zone, at a large distance of the source, beyond about mid-length. These waves are, however, perturbed near the longitudinal walls (those perpendicular to the circular source) due to reflections on these walls. These perturbations remain rather weak and do not perturb the main central part of the acoustic beam. It is why absorption conditions have not been applied at these boundaries. In contrast, since the acoustic beam is directed towards the right endwall, the waves remain rather intense in this end region. The non-reflecting conditions applied at this endwall are then really necessary to attenuate these waves and avoid their reflection and the occurrence of standing waves.

For comparison, the same situation is simulated in 2D, i.e. we consider a rectangular enclosure with dimensions $H = 240$ and $L = 320$, and a line of 81 point sources is located at mid-height of its left wall. The validation of this two-dimensional model has been widely discussed in our previous 2D works

[24,50]. Fig. 16 gives the longitudinal 2D and 3D density profiles plotted along the central x axis. We see that the two profiles have the same shape, but not the same amplitude. Indeed, the waves obtained in 2D and 3D are in phase and globally attenuated as they move away from the source. In the near field, however, the waves obtained in the 3D case have a larger amplitude than those obtained with a 2D simulation. This is due to the extra contribution of the point sources in the vicinity of the line of point sources considered in 2D.

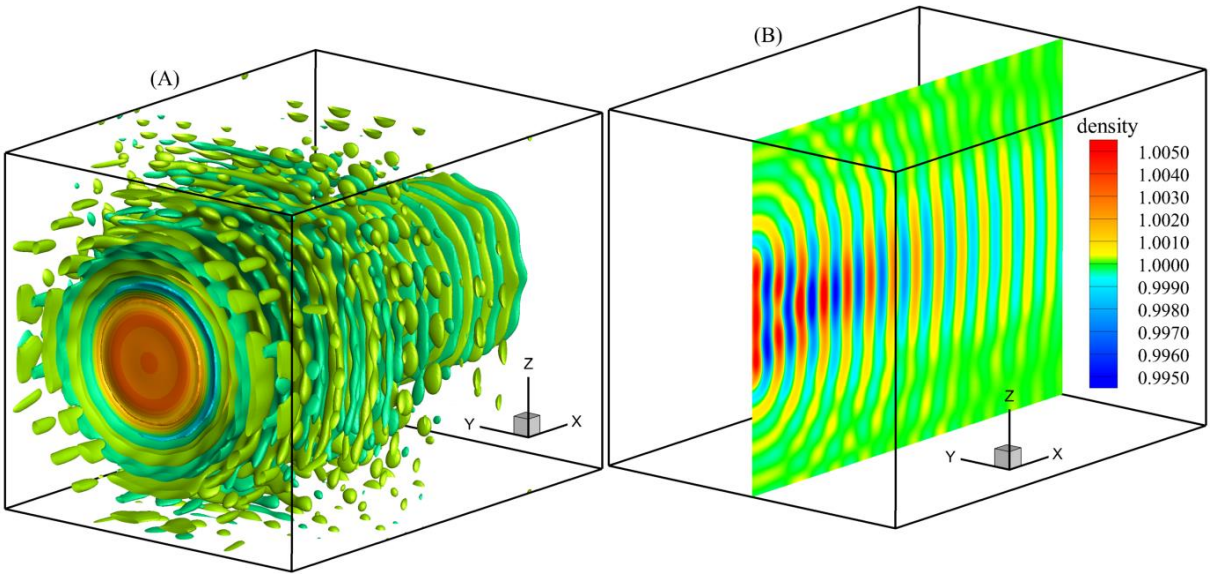

Fig. 15. Density field generated by a circular acoustic source at $t = 1100$: (A) 3D representation; (B) 2D depiction for a vertical section at $y = W/2$.

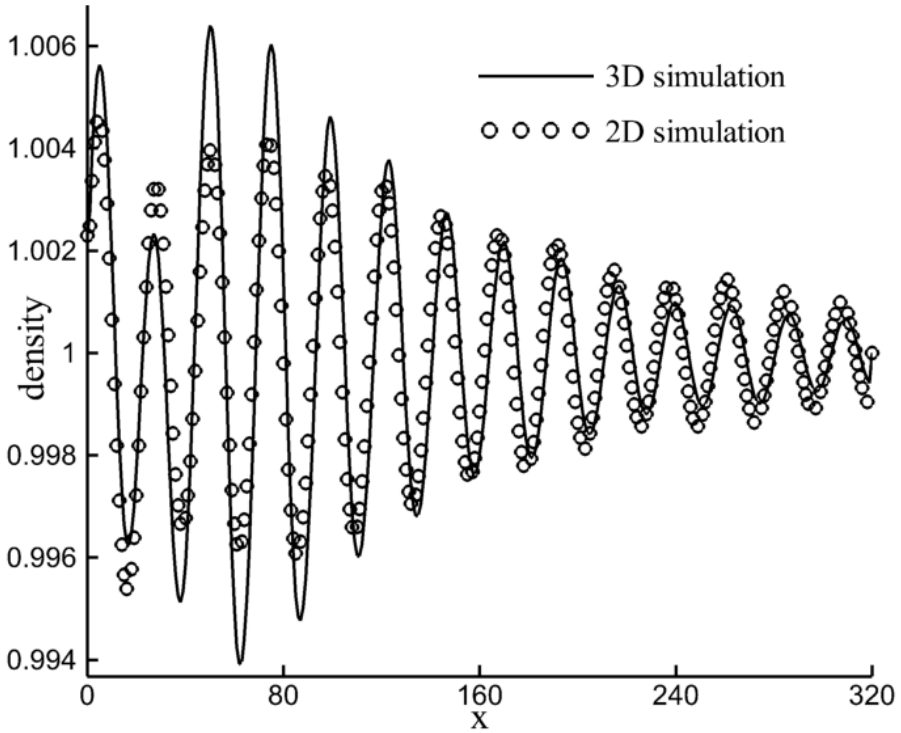

Fig. 16. Comparison of the longitudinal profiles of the density obtained at $t = 1100$ by 2D and 3D simulations of waves emitted by a source.

A velocity field is also generated in the enclosure as a result of the fluctuating density at the source. Since the direction of the waves propagation is along the x axis, the x component of the velocity (u) is

the main component. Fig. 17 shows the field of u at $t = 1100$. The flow is created by the sound source and therefore the velocity field itself takes the form of waves, with successively positive and negative velocities. As for the density, the strongest velocity amplitudes are found in the near field zone, with waves with a flat central front and curved sides. The spherical shape is only observed for the waves in the far-field zone, but it is also perturbed by the reflections on the longitudinal walls. Note that the field of u is also not perfectly axisymmetric. The transverse profile of the velocity u along the mid z axis (at $x = L/2, y = W/2$) is also plotted at two different times to observe the velocity fluctuations near the walls and at the center of the cavity (see Fig. 18). For example, at $t = 600$ (Fig. 18(A)), the velocity profile has a main positive peak around the central axis of the cavity (at $z = 120$), and smaller peaks, negative and then positive, closer to the walls. At $t = 1100$ (Fig. 18(B)), the profile of u is almost reversed. This could be expected, as the two states, separated by 12 and half periods, are in phase opposition. Note that the central peak has a positive value (at $t = 600$) stronger than the negative value (at $t = 1100$). This could be a sign of the streaming induced by the acoustic field, which is expected to be in the direction of the wave propagation (i.e. positive) along the central x axis. The study of the streaming will be the objective of our future works.

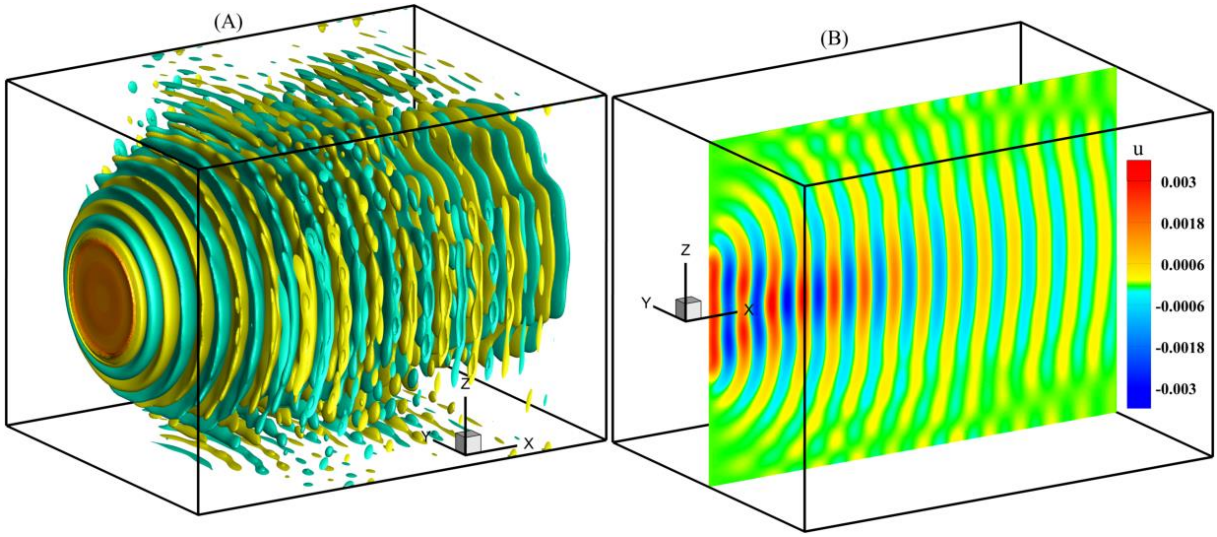

Fig. 17. Velocity field u generated by a circular acoustic source at $t = 1100$: (A) 3D representation; (B) 2D depiction for a vertical section at $y = W/2$.

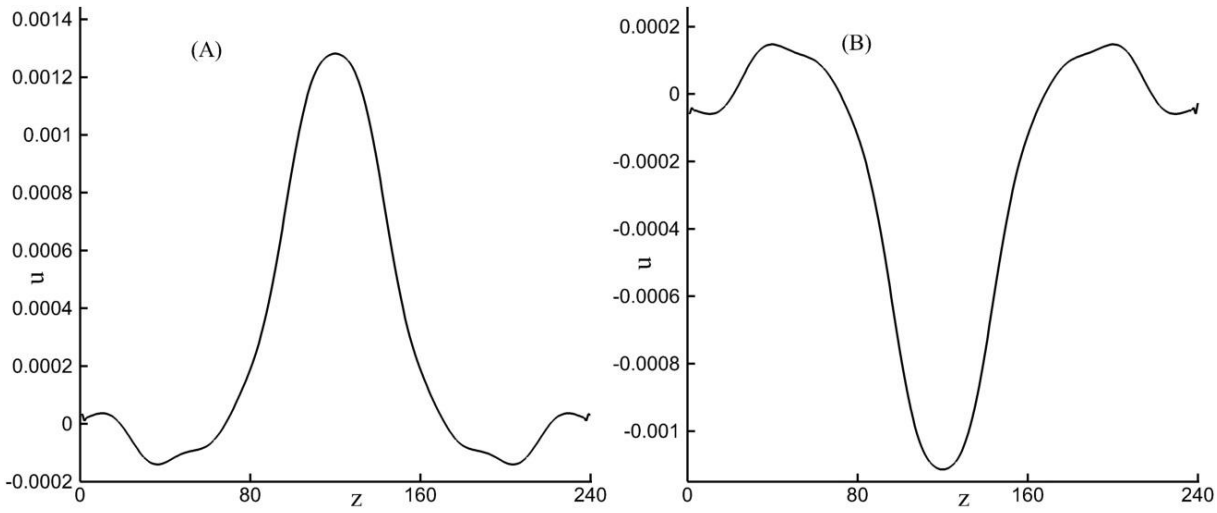

Fig. 18. Transverse profile of the velocity u along the mid z axis (at $x = L/2, y = W/2$) and at $t = 600$ (A) and 1100 (B).

In engineering, the calculation of the sound pressure is important, particularly in the case of acoustic streaming created by the propagation of waves generated by a transducer. Physically, the passage of sound waves through a fluid causes compression and decompression of the medium. This varying pressure is connected with the varying density. The variation of the density is described by the sinusoidal form of the out-of-equilibrium density ρ' (Eq. (20) or Eq. (22)) and the instantaneous pressure can be directly deduced from ρ' using the following relations:

$$p' = \rho' c_s^2 \quad \text{or} \quad p' = (\rho - \rho_0) c_s^2. \tag{30}$$

For a pressure wave expressed as $p' = p_{ac}\, cos(\omega t - kx)$, the amplitude p_{ac} can be directly calculated from the RMS value of the pressure p as:

$$p_{ac} = \sqrt{2 \langle p'^{\,2} \rangle}\,. \tag{31}$$

The term $\langle p'^{\,2} \rangle$ is calculated after the sound waves emitted by the sound source are well established throughout the cavity. Fig. 19 shows the sound pressure field averaged over a time interval of 10 periods T_{lbm} between iterations 700 and 1100. The three-dimensional structure of the pressure amplitude p_{ac} is illustrated in Fig. 19(A) and a vertical section at $y = W/2$ is depicted in Fig. 19(B). From these figures, it can be observed that the amplitude of the sound pressure takes important values in the first half of the cavity. Maxima are found on the source axis, close to the source and at the Fresnel length (near field: far-field boundary), and also outside the axis, around the minimum on the axis. The pressure amplitude then decreases in the far-field zone. The transverse profile along the mid y axis ($x = L/2$, $z = H/2$) is also given in Fig. 20. As expected for this profile taken in the far-field zone, the amplitude p_{ac} takes a maximum value at the center, with a large main peak surrounded by really smaller peaks when moving towards the sides.

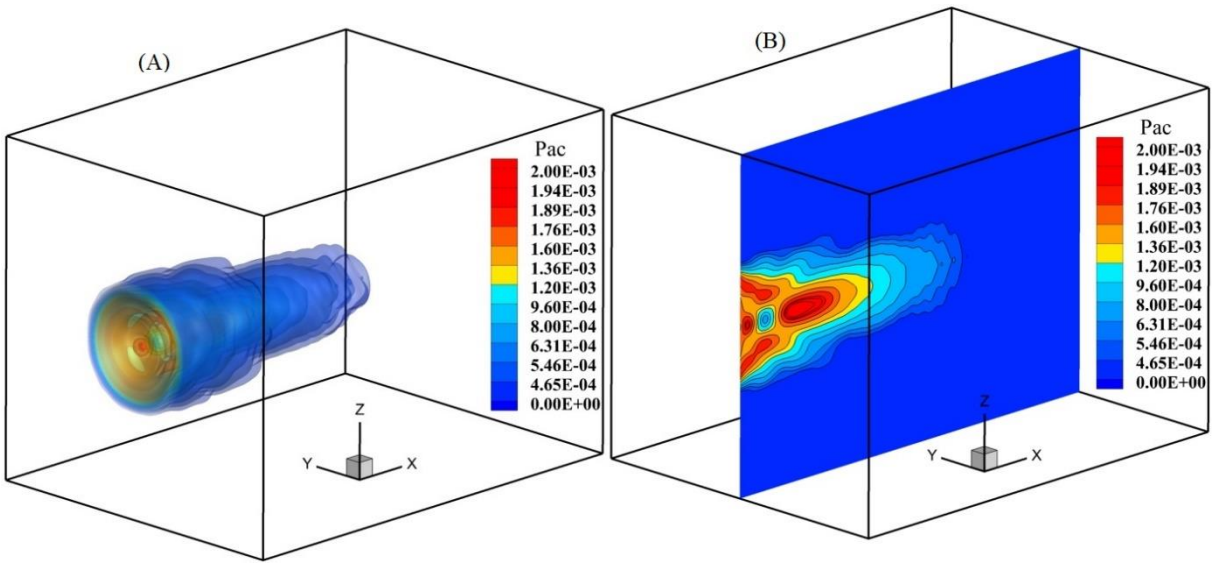

Fig. 19. Acoustic pressure amplitude p_{ac} generated by a circular acoustic source: (A) 3D representation; (B) 2D depiction for a vertical section at $y = W/2$.

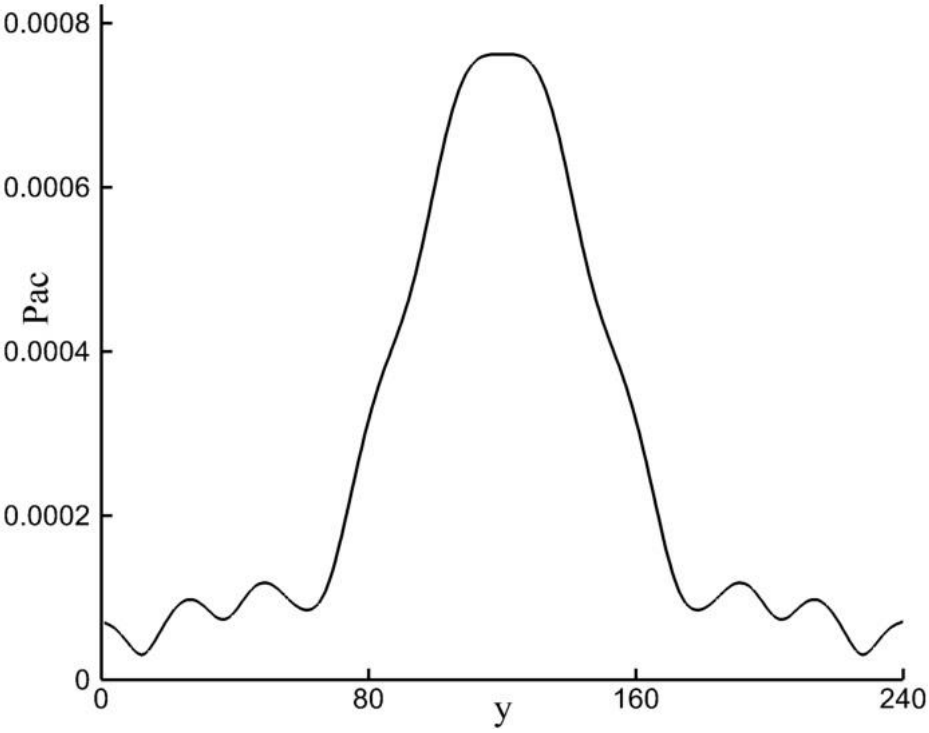

Fig. 20. Transverse profile along the mid y axis ($x = L/2$, $z = H/2$) for the acoustic pressure amplitude p_{ac} presented in Fig. 19.

To validate our 3D approach in the case of the circular acoustic source, it would be interesting to compare our results with analytical or experimental results, as it was done in a previous section for the single point source. An analytical expression of the pressure amplitude p_{ac} along the central axis of a circular vibrating piston can be found in [36]. This expression, which does not involve attenuation, can be written as:

$$p_{ac}(x) = p_{max}\left|sin\left(\frac{1}{2}\,k\,x\left(\sqrt{1+\left(\frac{a}{x}\right)^2}-1\right)\right)\right|, \tag{32}$$

where p_{max} is the maximum pressure without attenuation, which, for a baffled piston (as a transducer), is given as a function of equilibrium density, sound speed, and velocity amplitude u_a as $p_{max} = 2\rho_0 c_s u_a$ [36]. Basically, as mentioned in [51], factor 2 comes from the fact that the sound source is baffled and that all the radiation emitted by the source is forced into only half of the space (the free space ahead of the piston). In our case, we only consider the forward emission of the radiation inside the enclosure and this factor 2 has not to be introduced. To confirm this behavior, we have compared the waves generated by a point source placed, on one side, at the center of the cavity, and, on another side, at the center of the left wall. In both cases, it was found that the density oscillates between the same minimum and maximum values. Therefore, the maximum pressure amplitude in our case is given by:

$$p_{max} = \rho_0 c_s u_a. \tag{33}$$

Note that equation (32) does not consider the viscous attenuation effects of the waves. In the LBM approach, however, these effects are taken into account implicitly and will affect the different variables, as density, pressure, and velocities. Then, as for the analytical solution in the case of the spherical wave

(Eq. (26)), the dissipation of wave energy must be introduced in the analytical solution (32), with a factor $e^{(-\alpha x)}$. This finally gives:

$$p_{ac}(x) = p_{max} \left| sin\left(\frac{1}{2}\, k\, x \left(\sqrt{1 + \left(\frac{a}{x}\right)^2} - 1 \right) \right) \right| e^{(-\alpha x)}, \tag{34}$$

where, for a viscosity $\nu = 0.01$ and $\nu_B = 3\nu$, the value of the attenuation coefficient α given by (24) is $2.77\ 10^{-3}$.

The analytical result of the sound pressure amplitude given by Eq. (34) is shown in Fig. 21, together with the corresponding profile of p_{ac} obtained numerically. The two profiles of p_{ac} have the same spatial structure, with one peak in the near field, another peak at the Fresnel length, and a further decrease with the distance x in the far-field. The amplitude variations of the numerical profile, however, are clearly distinct from those of the analytical profile. Moreover, the value of p_{max} used in the analytical expression in Fig. 21 is 0.002, a value obtained by adjustment with the numerical profile. This value is different from the theoretical value given by Eq. (33), which is about 0.0033 (this value is calculated by defining the velocity amplitude as $u_a = c_s \rho_a = 0.0057$ [36]). Different ways are proposed in the following to improve our acoustic model in order to get a better fit of the numerical results with the analytical results.

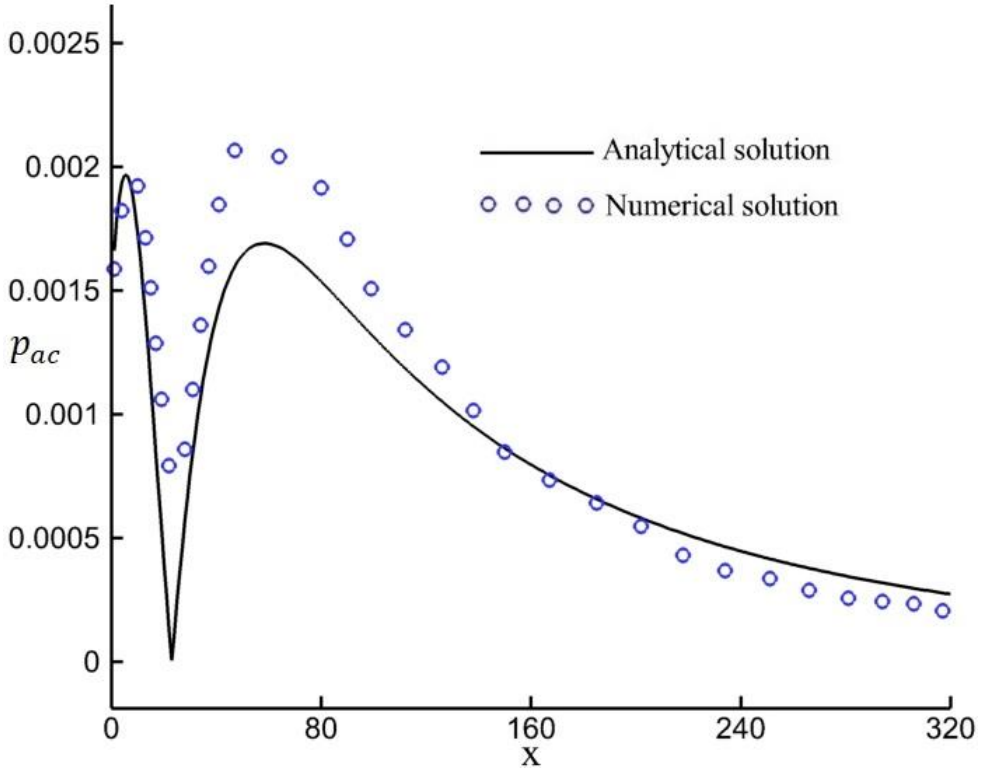

Fig. 21. Analytical (34) and numerical longitudinal profiles of sound pressure amplitude p_{ac} plotted along the central x axis in the case of the circular acoustic source, when the condition of wave emission is applied on the density and $s_1 = 1.19$. The p_{max} value used in the analytical expression is here obtained by adjustment with the numerical profile.

5.3.2 Discussion on the choice of the viscosity

To simulate the propagation of sound waves in the air using the D2Q9-SRT model, Salomons et al. [23] used a LBM kinematic viscosity $\nu = 0.06$. This viscosity value is significant and can lead to high attenuation. However, it has been used to stabilize the SRT model, as this model is unstable at low viscosity values. In contrast, with the MRT model, small viscosity values can be used, and this can be considered as a major advantage for the use of the MRT-LBM model.

In our study, the LBM kinematic viscosity found for water from Eq. (29) is very low ($\nu = 1.21\ 10^{-6}$) and therefore does not induce a high dissipation. As said before, the corresponding value of the attenuation coefficient given by (24) (with $\nu_B = 3\nu$) is very low ($\alpha = 3.35\ 10^{-7}$), which causes difficulties for the implementation of the absorbing boundary conditions (16) at the endwall. Then, the use of a relatively larger value of the viscosity is recommended. Moreover, numerically, the kinematic viscosity only enters into the calculation of the relaxation times ($s_9 = s_{11} = s_{13} = s_{14} = s_{15} = 1/(3\nu + 0.5)$), and its change from $1.21\ 10^{-6}$ to 0.01, for example, does not lead to a significant change of these parameters which keep a value in the vicinity of 2, so that similar results, particularly in terms of wave attenuation, are expected. As shown in Fig. 22, tests performed in the case of the circular acoustic source for kinematic viscosity of 0.01 instead of $1.21\ 10^{-6}$ confirm this fact: the longitudinal density profiles plotted along the central x axis at $t = 500$ are almost superimposed for the two cases, with only small differences at the top of the different oscillations. Thus, for reasons of reliability of our numerical LBM code, the viscosity of 0.01 is used instead of $1.21\ 10^{-6}$ in all the calculations performed in this work, and, as said before, the corresponding attenuation coefficient is $\alpha = 2.77\ 10^{-3}$, a value used in the analytical comparison using the equation (34).

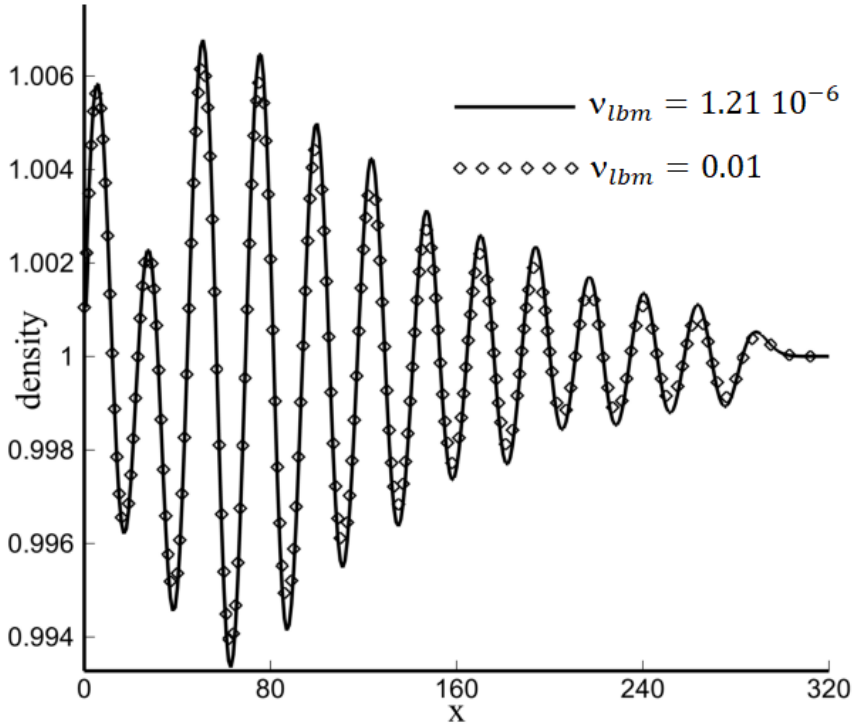

Fig. 22. Longitudinal density profiles along the central x axis at $t = 500$ for two values of the kinematic viscosity in the case of the circular acoustic source.

5.3.3 Velocity fluctuations applied at the source

For the vibration of a single point source, it was preferable to put the condition of wave emission on the density in order to take into account the propagation of waves in all directions. In contrast, for a surface vibrating in a single direction, as for a transducer, this condition could be as well put on the velocity. This choice even appears to be closer to the experimental conditions and is comforted by the mathematical expression of p_{max} for a transducer (Eq. (33)), which is expressed as a function of the velocity amplitude u_a. To test this possibility, we have modified the condition of wave emission, which is now:

$$u(t) = u_a \, sin(\omega t), \tag{35}$$

where u refers to the velocity along x, i.e. the transducer axis. To remain in similar conditions as in the previous sections (same value of p_{max}), the chosen velocity amplitude is $u_a = 0.0057$, the value deduced previously from ρ_a. The kinetic viscosity is kept at $\nu = 0.01$ and $s_1 = 1.19$.

The numerical profile of the pressure amplitude p_{ac} obtained with this new emission condition is given in Fig. 23 where it is compared with the analytical profile obtained from (34). The pressure profile obtained numerically is now closer to that calculated analytically, with, in particular, a good amplitude for the two peaks, but the dissipation in the far-field zone remains still too strong. Moreover, the value of p_{max} estimated from the numerical results ($p_{max} = 0.0028$) and used for the analytical profile in Fig. 23 is closer but still different from the theoretical value 0.0033 given by (33).

To still improve our numerical solution, we have to find a way to correct the too strong attenuation, particularly in the far-field zone. As mentioned in the previous sections and as indicated in the literature [23,37], in the LBM method, the two factors responsible for the attenuation of the waves are the viscous dissipation effect and the geometric spreading. Concerning the geometric spreading effect, it is proposed in [23] to improve its consideration by refining the mesh. This solution, which can be valid in 2D cases, is, however, of difficult use in 3D cases, as it is very costly in terms of computation time. Concerning the viscous dissipation effect, we come back to the characteristics of the MRT model. In this model, the effect of dissipation is integrated into several relaxation times, which depend on the kinematic viscosity ν ($s_9 = s_{11} = s_{13} = s_{14} = s_{15} = 1/(3\nu + 0.5)$). These times are well taken into account in our calculations, using the chosen viscosity ($\nu = 0.01$). A thorough survey of the literature, however, led us to find that there is another relaxation time, s_1, which also depends on the viscosity, but now the bulk viscosity ν_B. s_1 is defined in [28] as:

$$s_1 = \frac{2}{9\nu_B + 1}. \tag{36}$$

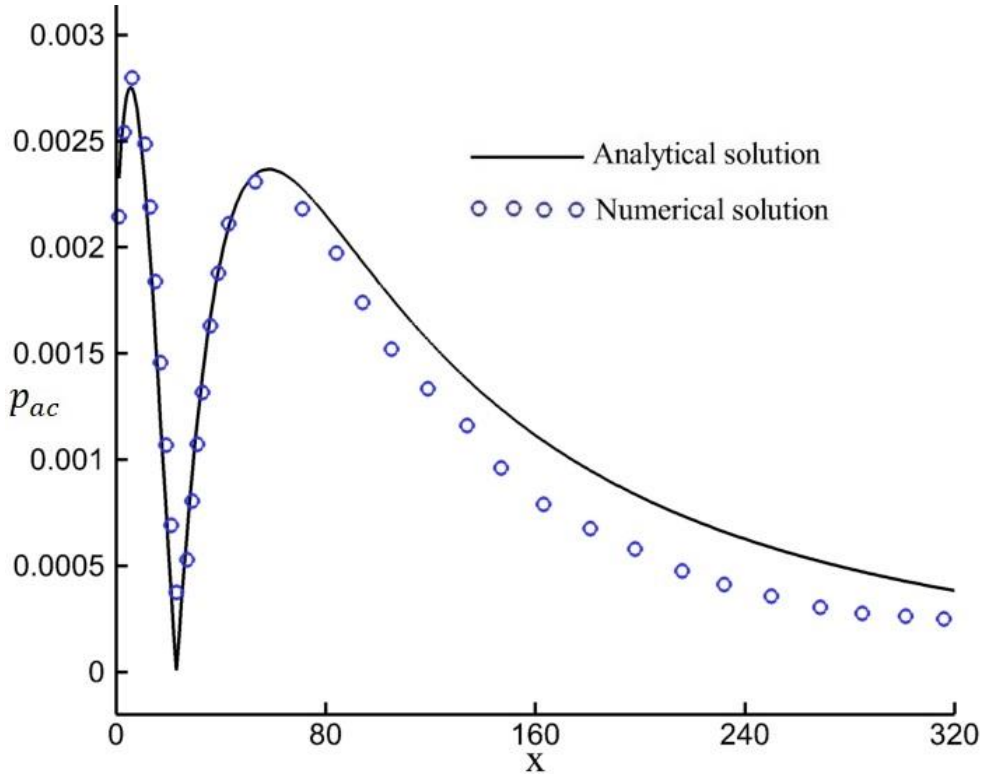

Fig. 23. Analytical (34) and numerical longitudinal profiles of sound pressure amplitude p_{ac} plotted along the central x axis in the case of the circular acoustic source, when the condition of wave emission is applied on the velocity and $s_1 = 1.19$. The p_{max} value used in the analytical expression is here obtained by adjustment with the numerical profile.

For $\nu_B = 3\nu = 0.03$, Eq. (36) gives a value of s_1 of about 1.57, a little stronger than the value 1.19 recommended in [28] and also used in [29]. Using this new value of s_1 instead of 1.19 significantly reduces the attenuation of the waves in the numerical LBM simulations of the circular source case. This is illustrated in Fig. 24, which represents the profile of the longitudinal velocity u along the central x axis for both values of s_1. Indeed, with $s_1 = 1.57$, the waves are less attenuated, especially in the far zone. Note that the value $s_1 = 1.19$ was recommended to have a stable model allowing the simulation of different problems of fluid mechanics [28]. Here, for the study of the propagation of acoustic waves in water, the value $s_1 = 1.57$, which seems more appropriate, remains numerically valid for the D3Q19 model, as no instability appears in the results. Further tests were performed by continuing to increase the value of s_1 to see its effect on the stability of our LBM model. These tests showed that our D3Q19 MRT scheme only becomes unstable for values of s_1 higher than 1.9: in these cases, clear perturbations are observed in the velocity profile along the central x axis.

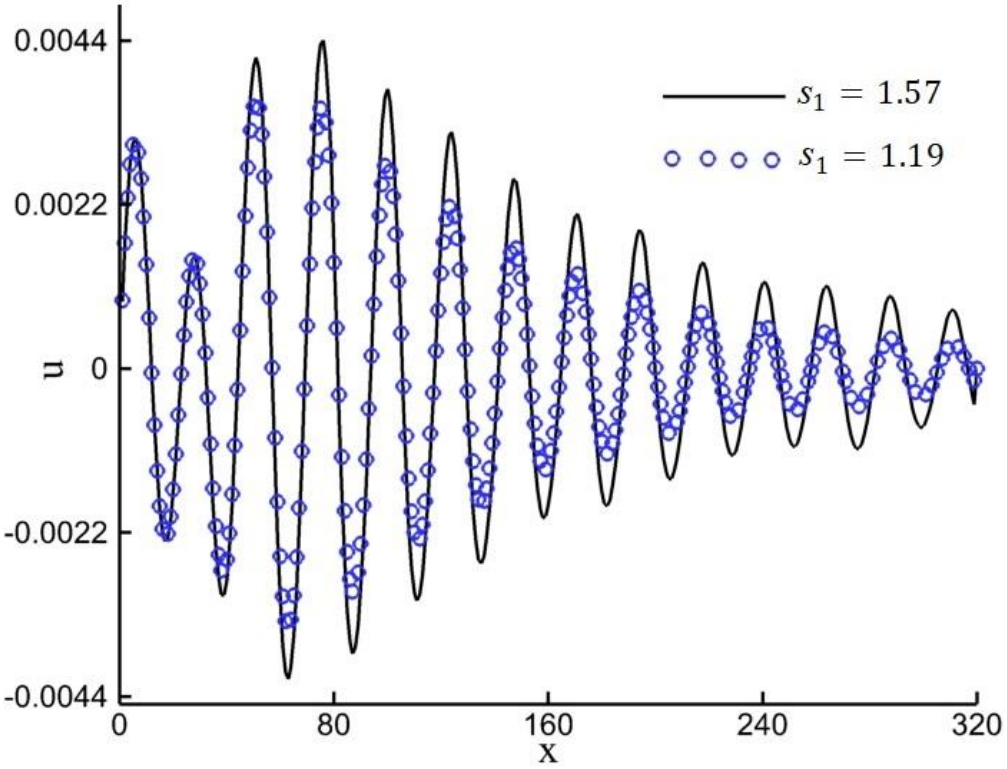

Fig. 24. Profiles of the longitudinal velocity u along the central x axis at $t = 1100$ for two values of the time relaxation s_1 in the case of the circular acoustic source.

Fig. 25 finally gives the numerical profile of the pressure amplitude p_{ac} along the central x axis for the case where the condition of wave emission is put on the velocity and the more appropriate value of s_1 given by the bulk viscosity ($s_1 = 1.57$) is used. In that case, the comparison with the analytical profile (34), which is not adjusted with the numerical results but uses the theoretical value of p_{max} given by (33) ($p_{max} = 0.0033$), is very good: the amplitude of the peak at the Fresnel length and the further decrease in the far-field zone are particularly well taken into account.

All these different studies allow us to conclude that the LBM method based on the D3Q19 MRT model is well adapted for the study of acoustic waves in 3D situations, and in particular waves emitted by a transducer. It can then be used with confidence to study different acoustic problems in the future.

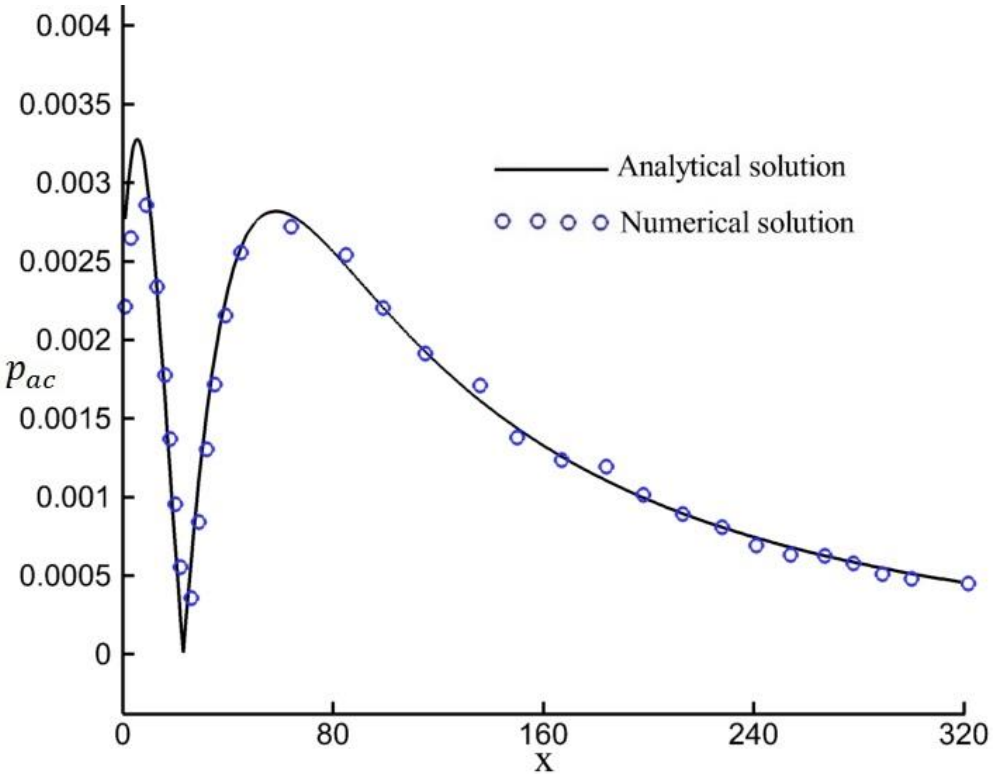

Fig. 25. Analytical (34) and numerical longitudinal profiles of sound pressure amplitude p_{ac} plotted along the central x axis in the case of the circular acoustic source, when the condition of wave emission is applied on the velocity and $s_1 = 1.57$. The p_{max} value used in the analytical expression is here the theoretical value given by (33) ($p_{max} = 0.0033$).

6. Conclusion

In previous works, we simulated the two-dimensional waves propagation phenomena by the lattice Boltzmann method (LBM) in the cases of a single point source and a line source. The results obtained were very precise and satisfactory but lacked comparisons with realistic situations. In the present work, our LBM code has been restructured to be able to simulate waves in three dimensions (3D).

As a first step, we started with the validation of our 3D model by simulating a lid-driven cavity flow: a good agreement was found between our results and those previously published in the literature. In a second step, we simulated the case of spherical waves emitted by a localized infinitesimal source and showed that sound waves can be easily produced with the point source technique.

From the perspective of acoustic streaming applications, our main objective was to study the case where the waves are emitted from a circular sound source (as the face of a transducer) placed at the center of the left boundary of a three-dimensional cavity filled with water. We first characterized the waves generated by such a source, using plots of the instantaneous density field and longitudinal velocity field. The results show that the waves propagate with a flat central front and curved sides near the source, in the near field zone where maximum wave amplitudes are found, whereas spherical shapes can be found in the far-field zone, at a large distance of the source, beyond about mid-length. These waves are numerically well absorbed at the surface opposite to the source by exploiting non-reflecting absorption conditions. The sound pressure amplitude in the cavity was also calculated by time-averaging the square of the instantaneous pressure. This allowed us to give the spatial structure of this pressure amplitude and to compare its values along the source axis with available analytical values for a circular piston. Different

tests led us to find the appropriate numerical conditions for a good comparison. The acoustic pressure amplitude resulting from a circular piston is first better reproduced by a condition of wave emission applied on the longitudinal velocity rather than on the density. Moreover, the right level of wave dissipation is obtained by using a relaxation time $s_1 = 1.57$, based on the value of the bulk viscosity, rather than the value $s_1 = 1.19$ recommended in the literature.

All these results highlight the performance of the lattice Boltzmann simulations in acoustics. They also give confidence in the possibility to use the LBM approach to simulate acoustic streaming, as in references [9,10].

Acknowledgements

This collaborative work was supported by the PHC Maghreb Partnership Program no. 36951NG and the Phase 2 PHC Toubkal Program. A grant to J.B. and the support from the PMCS2I of Ecole Centrale de Lyon for the numerical calculations are gratefully acknowledged.

References

[1] A. D. Pierce. Acoustics: An Introduction to Its Physical Principles and Applications. Springer, 2019. https://doi.org/10.1007/978-3-030-11214-1.

[2] E. A. Lopez-Poveda, R. Meddis. A physical model of sound diffraction and reflections in the human concha. The Journal of the Acoustical Society of America, 1996, vol. 100, no 5, p. 3248-32. https://doi.org/10.1121/1.417208.

[3] M. J. Buckingham. Sound Propagation. Applied Underwater Acoustics, 2017. p. 85-184. https://doi.org/10.1016/B978-0-12-811240-3.00002-3.

[4] M. J. Crocker. Handbook of Noise and Vibration Control. John Wiley & Sons, 2007. https://doi.org/10.1002/9780470209707.

[5] F. Jacobsen, T. Poulsen, J. H. Rindel, A. C. Gade, M. Ohlrich. Fundamentals of Acoustics and Noise Control. Technical University of Denmark, Department of Electrical Engineering, 2011.

[6] J. Blauert, N. Xiang. Acoustics for Engineers: Troy Lectures. Springer Science & Business Media, 2009. https://doi.org/10.1007/978-3-642-03393-3.

[7] T. Leong, L. Johansson, P. Juliano, S.L. McArthur, R. Manasseh. Ultrasonic separation of particulate fluids in small and large scale systems: A review. Industrial & Engineering Chemistry Research, 2013, vol. 52, no 47, p. 16555-16576. https://doi.org/10.1021/ie402295r.

[8] M. C. Charrier-Mojtabi, X. Jacob, T. Dochy, A. Mojtabi. Species separation of a binary mixture under acoustic streaming. The European Physical Journal E, 2019, vol. 42, no 5, p. 1-8. https://doi.org/10.1140/epje/i2019-11824-9.

[9] B. Moudjed. Caractérisation expérimentale et théorique des écoulements entraînés par ultrasons. Perspectives d' utilisation dans les procédés de solidification du Silicium Photovoltaïque. Doctoral thesis, INSA Lyon, France, 2013.

[10] B. Moudjed, V. Botton, D. Henry, H. Ben Hadid, J. P. Garandet. Scaling and dimensional

analysis of acoustic streaming jets. Physics of Fluids, 2014, vol. 26, no 9, p. 093602. https://doi.org/10.1063/1.4895518.

[11] D. Ensminger, L. J. Bond. Ultrasonics : fundamentals, technologies, and applications. CRC Press, 2011. https://doi.org/10.1201/b11173.

[12] A. K. W. Wood, C. M. Sehgal. A review of low-intensity ultrasound for cancer therapy. Ultrasound in medicine & biology, 2015, vol. 41, no 4, p. 905-928. https://doi.org/10.1016/j.ultrasmedbio.2014.11.019.

[13] S. V Ranganayakulu, N. R. Rao, L. Gahane. Ultrasound applications in Medical Sciences. IJMTER, 2016, vol. 3, p. 287-93.

[14] U. Frisch, B. Hasslacher, Y. Pomeau. Lattice-gas automata for the Navier-Stokes equation. Physical review letters, 1986, vol. 56, no 14, p. 1505. https://doi.org/10.1103/PhysRevLett.56.1505.

[15] G. R. McNamara, G. Zanetti. Use of the Boltzmann equation to simulate lattice-gas automata. Physical review letters, 1988, vol. 61, no 20, p. 2332. https://doi.org/10.1103/PhysRevLett.61.2332.

[16] X. He, L. S. Luo. Theory of the lattice Boltzmann method: From the Boltzmann equation to the lattice Boltzmann equation. Physical Review E, 1997, vol. 56, no 6, p. 6811. https://doi.org/10.1103/PhysRevE.56.6811.

[17] A. A. Mohamad. Lattice Boltzmann Method: Fundamentals and Engineering Applications with Computer Codes. Springer, 2011. https://doi.org/10.1007/978-0-85729-455-5.

[18] K. Timm, H. Kusumaatmaja, A. Kuzmin, O. Shardt, G. Silva, E. Viggen. The Lattice Boltzmann Method: Principles and Practice. Springer International Publishing AG Switzerland, 2017. https://doi.org/10.1007/978-3-319-44649-3.

[19] H. Huang, M. Sukop, X. Lu. Multiphase Lattice Boltzmann Methods: Theory and Application. John Wiley & Sons, 2015. https://doi.org/10.1002/9781118971451.

[20] Y. Guangwu, C. Yaosong, H. Shouxin. Simple lattice Boltzmann model for simulating flows with shock wave. Physical Review E, 1999, vol. 59, no 1, p. 454. https://doi.org/10.1103/PhysRevE.59.454.

[21] S. Xiao. A lattice Boltzmann method for shock wave propagation in solids. Communications in numerical methods in engineering, 2007, vol. 23, no 1, p. 71-84. https://doi.org/10.1002/cnm.883.

[22] J. M. Buick, C. A. Greated, D. M. Campbell. Lattice BGK simulation of sound waves. EPL (Europhysics Letters), 1998, vol. 43, no 3, p. 235. https://doi.org/10.1209/epl/i1998-00346-7.

[23] E. M. Salomons, W. J. A. Lohman, H. Zhou. Simulation of sound waves using the lattice Boltzmann method for fluid flow: Benchmark cases for outdoor sound propagation. PloS one, 2016, vol. 11, no 1, p. e0147206. https://doi.org/10.1371/journal.pone.0147206.

[24] J. Benhamou, M. Jami, A. Mezrhab, V. Botton, D. Henry. Numerical study of natural convection and acoustic waves using the lattice Boltzmann method. Heat Transfer, 2020, vol. 49, no 6, p. 3779-3796. https://doi.org/10.1002/htj.21800.

[25] P. Lallemand, L. S. Luo. Theory of the lattice Boltzmann method: Acoustic and thermal properties in two and three dimensions. Physical review E, 2003, vol. 68, no 3, p. 036706. https://doi.org/10.1103/PhysRevE.68.036706.

[26] S. Chen, Z. Wang, X. Shan, G. D. Doolen. Lattice Boltzmann computational fluid dynamics in three dimensions. Journal of Statistical Physics, 1992, vol. 68, no 3, p. 379-400. https://doi.org/10.1007/BF01341754.

[27] N. S. Martys, H. Chen. Simulation of multicomponent fluids in complex three-dimensional geometries by the lattice Boltzmann method. Physical Review E, 1996, vol. 53, no 1, p. 743. https://doi.org/10.1103/PhysRevE.53.743.

[28] D. D'Humières, I. Ginzburg, M. Krafczyk, P. Lallemand, L.S. Luo. Multiple-relaxation-time lattice Boltzmann models in three dimensions. Philosophical Transactions of the Royal Society of London. Series A: Mathematical, Physical and Engineering Sciences, 2002, vol. 360, no 1792, p. 437-451. https://doi.org/10.1098/rsta.2001.0955.

[29] Z. Li, M. Yang, Y. Zhang. Lattice Boltzmann Method Simulation of 3-D Natural Convection with Double MRT Model. International Journal of Heat and Mass Transfer, 2016, vol. 94, p. 222-238. https://doi.org/10.1016/j.ijheatmasstransfer.2015.11.042.

[30] Y. Hu, D. Li, S. Shu, X. Niu. Lattice Boltzmann simulation for three-dimensional natural convection with solid-liquid phase change. International Journal of Heat and Mass Transfer, 2017, vol. 113, p. 1168-1178. https://doi.org/10.1016/j.ijheatmasstransfer.2017.05.116.

[31] Q. Liu, X. Feng, Y. He, C. Lu, Q. Gu. Three-dimensional multiple-relaxation-time lattice Boltzmann models for single-phase and solid-liquid phase-change heat transfer in porous media at the REV scale. Applied Thermal Engineering, 2019, vol. 152, p. 319-337. https://doi.org/10.1016/j.applthermaleng.2019.02.057.

[32] K. Ghasemi, M. Siavashi. Three-dimensional analysis of magnetohydrodynamic transverse mixed convection of nanofluid inside a lid-driven enclosure using MRT-LBM. International Journal of Mechanical Sciences, 2020, vol. 165, p. 105199. https://doi.org/10.1016/j.ijmecsci.2019.105199.

[33] L. M. Yang, C. Shu, Z. Chen, J. Wu. Three-dimensional lattice Boltzmann flux solver for simulation of fluid-solid conjugate heat transfer problems with curved boundary. Physical Review E, 2020, vol. 101, no 5, p. 053309. https://doi.org/10.1103/PhysRevE.101.053309.

[34] A. Xu, T. S. Zhao, L. An, L. Shi. A three-dimensional pseudo-potential-based lattice Boltzmann model for multiphase flows with large density ratio and variable surface tension. International Journal of Heat and Fluid Flow, 2015, vol. 56, p. 261-271. https://doi.org/10.1016/j.ijheatfluidflow.2015.08.001.

[35] Q. Li, D. H. Du, L. L. Fei, K. H. Luo. Three-dimensional non-orthogonal MRT pseudopotential lattice Boltzmann model for multiphase flows. Computers & Fluids, 2019, vol. 186, p. 128-140.

https://doi.org/10.1016/j.compfluid.2019.04.014.

[36] L. E. Kinsler, A. R. Frey, A. B. Coppens, J. V. Sanders. Fundamentals of Acoustics, 4th Edition. John wiley & sons, 2000.

[37] E. M. Viggen. The lattice Boltzmann method with applications in acoustics. Master's thesis, Norges teknisk-naturvitenskapelige universitet, Fakultet for naturvitenskap og teknologi, Institutt for fysikk, 2009.

[38] M. Jami, F. Moufekkir, A. Mezrhab, J. P. Fontaine, M. Bouzidi. New thermal MRT lattice Boltzmann method for simulations of convective flows. International Journal of Thermal Sciences, 2016, vol. 100, p. 98-107. https://doi.org/10.1016/j.ijthermalsci.2015.09.011.

[39] A. Mezrhab, M. Amine Moussaoui, M. Jami, H. Naji, M. Bouzidi. Double MRT thermal lattice Boltzmann method for simulating convective flows. Physics Letters A, 2010, vol. 374, no 34, p. 3499-3507. https://doi.org/10.1016/j.physleta.2010.06.059.

[40] K. N. Premnath, J. Abraham. Three-Dimensional Multi Relaxation Time (MRT) Lattice-Boltzmann Models for Multiphase Flow. Journal of Computational Physics, 2007, vol. 224, no 2, p. 539-559. https://doi.org/10.1016/j.jcp.2006.10.023.

[41] D. Heubes, A. Bartel, M. Ehrhardt. Characteristic boundary conditions in the lattice Boltzmann method for fluid and gas dynamics. Journal of Computational and Applied Mathematics, 2014, vol. 262, p. 51-61. https://doi.org/10.1016/j.cam.2013.09.019.

[42] D. Haydock, J. M. Yeomans. Lattice Boltzmann simulations of attenuation-driven acoustic streaming. Journal of Physics A: Mathematical and General, 2003, vol. 36, no 20, p. 5683. https://doi.org/10.1088/0305-4470/36/20/322.

[43] H. C. Ku, R. S. Hirsh, T. D. Taylor. A pseudospectral method for solution of the three-dimensional incompressible Navier-Stokes equations. Journal of Computational Physics, 1987, vol. 70, no 2, p. 439-462. https://doi.org/10.1016/0021-9991(87)90190-2.

[44] B. N. Jiang, T. L. Lin, L. A. Povinelli. Large-scale computation of incompressible viscous flow by least-squares finite element method. Computer Methods in Applied Mechanics and Engineering, 1994, vol. 114, no 3-4, p. 213-231. https://doi.org/10.1016/0045-7825(94)90172-4.

[45] H. Ding, C. Shu, K. S. Yeo, D. Xu. Numerical computation of three-dimensional incompressible viscous flows in the primitive variable form by local multiquadric differential quadrature method. Computer Methods in Applied Mechanics and Engineering, 2006, vol. 195, no 7-8, p. 516-533. https://doi.org/10.1016/j.cma.2005.02.006.

[46] M. Bouzidi, M. Firdaouss, P. Lallemand. Momentum transfer of a Boltzmann-lattice fluid with boundaries. Physics of fluids, 2001, vol. 13, no 11, p. 3452-3459. https://doi.org/10.1063/1.1399290.

[47] S. De, K. Nagendra, K. N. Lakshmisha. Simulation of laminar flow in a three-dimensional lid-driven cavity by lattice Boltzmann method. International Journal of Numerical Methods for Heat & Fluid Flow, 2009, Vol. 19 No. 6, pp. 790-815. https://doi.org/10.1108/09615530910973011.

[48] Y. Wang, C. Shu, C. J. Teo, J. Wu, L. Yang. Three-Dimensional Lattice Boltzmann Flux Solver and Its Applications to Incompressible Isothermal and Thermal Flows. Communications in Computational Physics, 2015, vol. 18, no 3, p. 593-620. https://doi.org/10.4208/cicp.300514.160115a.

[49] E. M. Viggen. The lattice Boltzmann method: Fundamentals and acoustics. Ph.D. thesis, Norwegian University of Science and Technology, Trondheim, Norway, 2014.

[50] J. Benhamou, M. Jami, A. Mezrhab. Application of the Lattice Boltzmann Method to the Acoustic Wave in a Rectangular Enclosure. In Proceedings of the 2nd International Conference on Advanced Technologies for Humanity - ICATH, 42-47, 2020, Rabat, Morocco. https://doi.org/10.5220/0010427200420047.

[51] D. T. Blackstock. Fundamentals of physical acoustics. The Journal of the Acoustical Society of America, 2001. https://doi.org/10.1121/1.1354982.